Pergamon

Int. J. Solids Structures Vol. 35, No. 36, pp. 5051–5083, 1998

Printed in Great Britain
0020-7683/98/$—see front matter

PII: S0020-7683(97)00248-5

THE MULTI-FRACTURE RESPONSE OF CROSS-PLY CERAMIC COMPOSITES

D. L. ERDMAN and Y. WEITSMAN*

Department of Mechanical and Aerospace Engineering and Engineering Science, The University of Tennessee, 307 Perkins Hall, Knoxville, TN 37996-2030, U.S.A. and Oak Ridge National Laboratory, Oak Ridge, TN 37831-8051, U.S.A.

(*Received* 5 *March* 1996; *in revised form* 31 *July* 1997)

Abstract—The mechanical response of cross-ply SiC/CAS ceramic matrix composites was investigated experimentally and analytically. The experiments consisted of recording stress–strain behavior, counting matrix cracks and measuring the interlaminar shearing strength. The analysis employed an extended shear-lag model which incorporated non-linear behavior of the 0° plies and interlaminar slip between the 0 and 90° plies. The evolution of the multi-cracking process was determined by means of fracture criterion, leading to the prediction of the overall stress–strain response of the cross-ply laminate. © 1998 Elsevier Science Ltd. All rights reserved.

1. INTRODUCTION

Ceramic materials retain their load bearing properties at temperatures that are much higher than levels that are admissible for metals and polymers. The major limitation on the mechanical performance of monolithic ceramics, which is their excessive brittleness resulting in low levels of strain at failure, can be overcome by the incorporation of relatively ductile fibers into the ceramic matrix. Since unidirectional reinforcement enhances ductility in the fiber direction, but does little to overcome brittleness in the transverse direction it is necessary to utilize multi-directional reinforcement for structural applications. The simplest circumstance of such reinforcement is represented by cross-ply laminates where fibers in distinct plies are oriented perpendicularly to each other.

The listing and summary of reference literature concerned with the very active field of ceramic composites is beyond the scope of this work. However, a comprehensive list of references which includes an overview of research on unidirectionally reinforced ceramics and an evaluation of works on cross-ply composites can be found in a recent publication (Erdman, 1995). It suffices to say that the list of references can be divided into three groups that focus primarily on modeling, modeling supported by experimental work, and experimental studies. In most cases the aforementioned investigations were concerned with detailed studies of specific micro-mechanisms. In fewer circumstances (e.g. Zhu and Weitsman, 1994) a model was developed to account for the overall stress–strain response of the uni-directional composite, by accounting for multiple fractures.

The situation is less satisfactory in the case of ceramic matrix cross-ply laminates. Some of these works employ shear-lag models developed for polymeric cross-ply laminates (e.g., Nuismer and Tan, 1988, 1989; Lee and Daniel, 1990) in spite of their obvious limitations when applied to the ceramic case, caused by the fact that the foregoing models disregard the pronounced non-linearity of the 0° plies and the presence of slippage at the 0/90° interface. In some articles the latter effects are treated in an *ad hoc* manner.

As will be shown in this article, the determination of the interfacial shearing strength between the 0 and 90° plies provides a crucial parameter for the modeling of the response of cross-ply laminates. While measurements of the interfacial shearing strength between the fiber and matrix in ceramic composites abound in the literature, together with accompanying mechanics models (see Erdman, 1995 for a listing of articles concerned with fiber/matrix interface studies) there seems to exist only a single work concerned with the interlaminar

* Author to whom correspondence should be addressed. Tel.: 001 423 974 5460. Fax: 001 423 974 6394. E-mail: weitsmana@utk.edu.

shearing strength (Wu *et al.*, 1993). However, that work did not provide information for SiC/CAS ceramic composites, which is required for the present work.

The purpose of this article is to elucidate the global stress–strain response of cross-ply ceramic composites by accounting for, then averaging, the micro-level effects. Therefore, only macro-level stress–strain behavior of the 0° plies is considered and interactions between micro-level fractures in the 0 and 90° plies are ignored. Some accounting for such micro-level interactions were attempted recently (Yu *et al.*, 1995).

2. EXPERIMENTAL

2.1. *Materials and experimental set-up*

Mechanical tests were performed on two ceramic matrix composite crossply lay-ups, $[0_2/90_2]_s$ and $[0_2/90_4]_s$ consisting of SiC/CAS (Nicalon fiber/Calcium alumino silicate glass ceramic matrix). Test coupons of $15.2 \times 1.27 \times 0.165$ and $15.2 \times 1.27 \times 0.24$ cm, respectively, were machined from laminated plates. The specimens were tabbed with tapered glass/epoxy (G-10) to minimize stress concentrations, and the specimen edges were polished to facilitate observation of microscopic damage progression under load.

Testing was conducted on MTS 50 Kip servo-hydraulic test system with 442 controllers and Microprofiler function generator. Instron "Supergrips" were used in conjunction with Instron mechanical wedge action grips to minimize the effects of bending and torsion on the specimen and provide clamping in a controlled manner. An Olympus BH2 optical microscope mounted on a *XYZ* platform was used in conjunction with a digital chip camera to record all activity on the specimen surface during load application. This video system was connected to a VHS format video cassette recorder to save all test records in real time as load was applied. The final magnification of this video system was approximately 750×. A schematic representation of the test set-up is shown in Fig. 1.

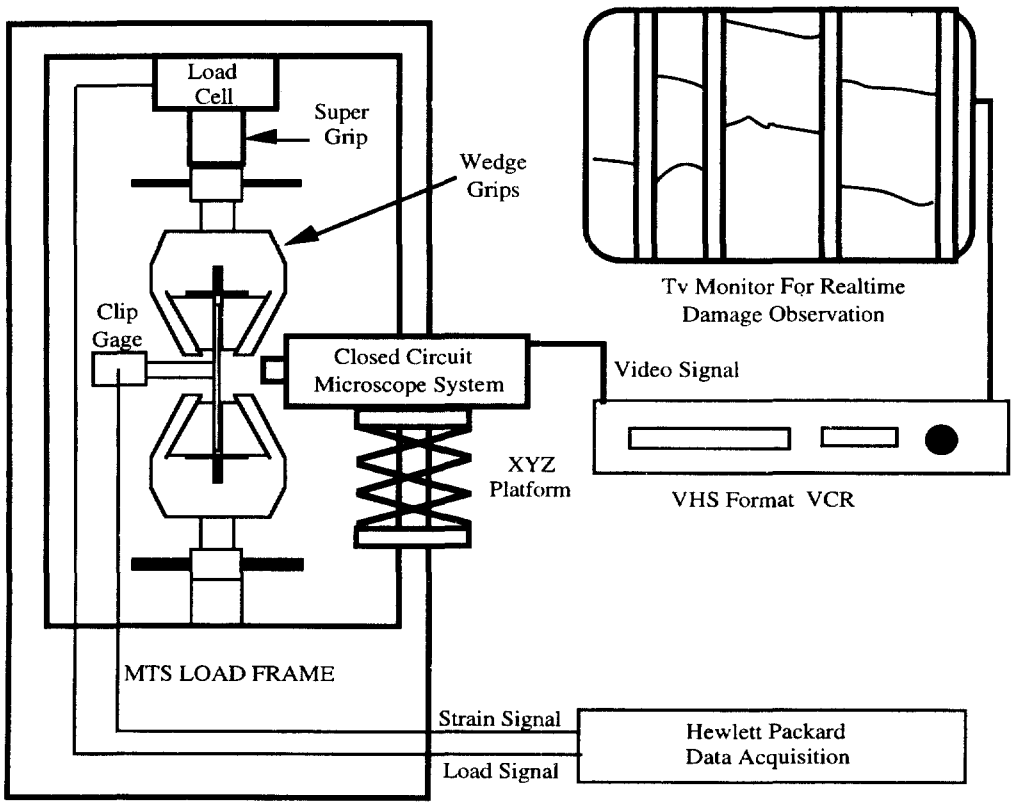

Fig. 1. Experimental set-up.

All tests were conducted in stroke (displacement) control at a loading rates between 0.003 and 0.010 in/min. An MTS 632 extensometer with a one inch gage length was used to monitor strain. To collect stress–strain data, the specimens were loaded continuously to failure while load and strain signals were recorded using an HP3497 data acquisition/control unit. To determine crack densities as a function of applied stress, it was necessary to interrupt the loading intermittently at pre-determined stress levels. During these stages, the surface of the specimen was scanned for evidence of damage. The stress and strain levels were then recorded to correlate observed damage with specific points on the stress–strain curve. It should be noted that the stress–strain curves for both the continuous and intermittent tests were in close agreement.

2.2. *Damage mechanisms and stress–strain response of cross-ply ceramic matrix laminates*

The overall response of cross-ply laminates reflects the behavior of the 0° plies and the additional mechanisms introduced by the presence of the 90° plies and the 0/90° interfaces.

The stress–strain behavior of the 0° plies exhibits substantial non-linearity as shown in Fig. 2. The mechanisms that account for the above non-linearity consist of matrix cracking bridged by intact fibers, which is accompanied by fiber/matrix interfacial debonds and slippage. At higher load levels fiber fragmentation and pull-out occurs. However, in this investigation a laminate-level model is constructed from ply level behavior. Therefore, the response of the unidirectional layer is treated as a "lumped" property to be incorporated within the cross-ply model. Consequently, the current analysis overlooks the detailed mechanisms within the 0° plies which were treated by Weitsman and Zhu (1993, 1994).

The additional mechanisms characteristic to cross-ply laminates are transverse cracks in the 90° ply groups and interfacial slip at the 0/90° interfaces. Typical micrographs of transverse cracks are shown in Figs 3(a) and (b). Note that at lower stress levels the crack in the 90° ply terminates at the interface, while at higher stress levels these cracks are accompanied by a multitude of cracks in the 0° plies. In many cases, the latter cracks are clustered in the neighborhood of a transverse crack in the 90° as shown in Fig. 4.

Typical stress–strain and crack density data are shown in Figs 5(a) and (b). It is worth noting that while the stress–strain curves show remarkable reproducibility, the crack density data exhibit substantial scatter. At least in part, this scatter is due to the presence of

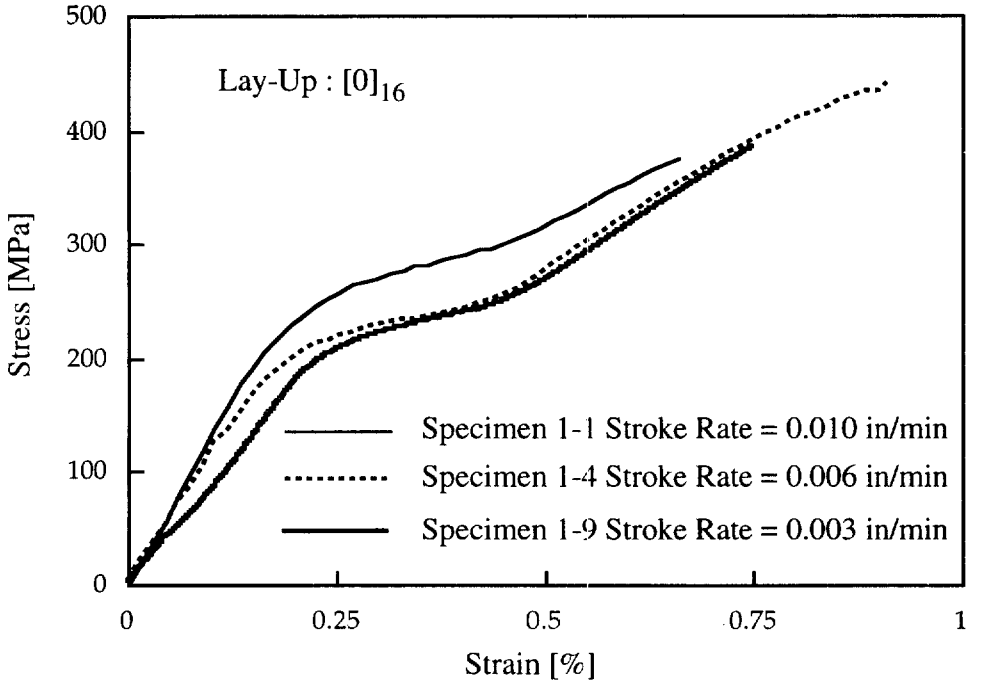

Fig. 2. Stress–strain response of unidirectional ceramic matrix composites.

discontinuous, meandering and partial cracks which are difficult to positively identify, hence the observed crack density is somewhat subjective. A listing of crack density data is given in Table 1.

Although some evidence of inter-ply interfacial slip may be discerned from micrographs such as in Fig. 4, such evidence does not provide the quantitative information required for the modeling of the mechanical response. Therefore an assessment of the magnitude of the interfacial shearing strength, τ_s^*, was obtained with the aid of a custom made "mini-shear" testing fixture sketched in Fig. 6.

This fixture is designed to be installed between the actuator and the crosshead of any standard testing machine that can accommodate flat platens. The specimen, which consist of a $[0_n/90_m]_s$ lay-up, is inserted in the fixture, with the outer 0° plies constrained against motion while the inner, 90° ply group, is pushed forward by the anvil. The load and displacement of the anvil are then monitored throughout the test. It should be noted that a very small specimen is required to avoid buckling and reduce misalignment in order to minimize any uneven shearing stresses at the two 0/90° interfaces. Typical specimen dimensions were $6.2 \times 6.2 \times 1.65$ mm. In some cases the length of the specimen (parallel to the load direction) was reduced to 3.1 mm. A typical load displacement record is shown in Fig. 7.

It should be noted that the "mini-shear" test yields inaccurate results since specimen thicknesses vary and the 0/90° interface is not clearly defined. Consequently, it was not possible to obtain a precise match between the widths of the die and the 90° ply group, which resulted in stress concentrations near the corners of the specimen where it was supported by the die, as can be seen in Fig. 8. These stress concentrations undoubtedly yielded lower than actual values for the interfacial shearing strength, τ_s^*. Nevertheless, an average experimental value of approximately 35 MPa was obtained from a series of eighteen tests, which seems to provide a reasonable order of magnitude for τ_s^* to be employed in the predictive model. It should be noted that due to data scatter we had $27 \text{ MPa} < \tau_s^* < 54 \text{ MPa}$.

3. ANALYSIS

3.1. *Linear elastic case*

Consider a ceramic cross-ply laminate as shown in Fig. 9 with exterior layers of 0° plies and interior 90° plies. An average axial stress, $\bar{\sigma}_x$, is applied to the laminate resulting in the cracking of the 90° plies. The crack spacing, $2L$, is assumed to be uniform along the length of the specimen.

In the sequel we shall employ the shear-lag method to derive approximate expressions for the stress and displacement fields for the cracked geometry. Let $i = 1, 2$ refer to the 90 and 0° ply groups, respectively. Then employing standard notation, we assume

$$u_1(x, z_1) = f(x)\left[a_1 + c_1\left(\frac{z_1}{h_1}\right)^2\right] \qquad 0 \leqslant z_1 \leqslant h_1$$

$$u_2(x, z_2) = f(x)\left[a_2 + b_2\left(\frac{z_2}{h_2}\right) + c_2\left(\frac{z_2}{h_2}\right)^2\right] \qquad 0 \leqslant z_2 \leqslant h_2 \tag{1}$$

In addition, the transverse displacements are taken to be

$$v_1 = v_2 = y\bar{\varepsilon}_y \tag{2}$$

and the out-of-plane effects are discarded. Consequently, the shear stresses are given as:

(a)

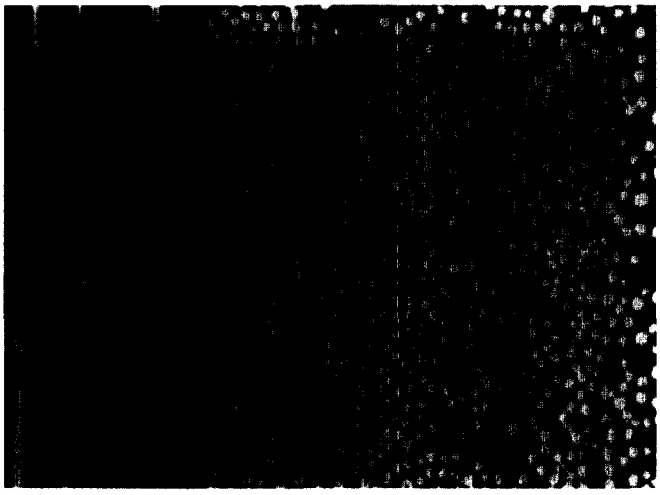

Fig. 3a. A single transverse crack in the 90° ply group shortly after matrix crack initiation.

(b)

Fig. 3b. Multiple transverse cracks in the 0 and 90° ply groups prior to laminate failure.

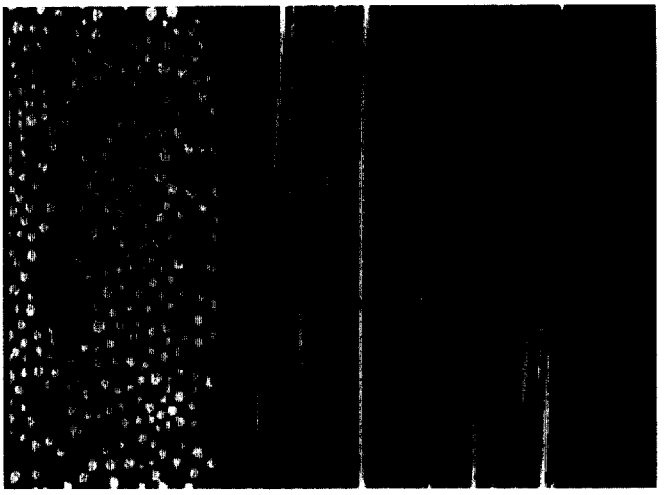

Fig. 4. Transverse crack "clusters" in the 0° plies.

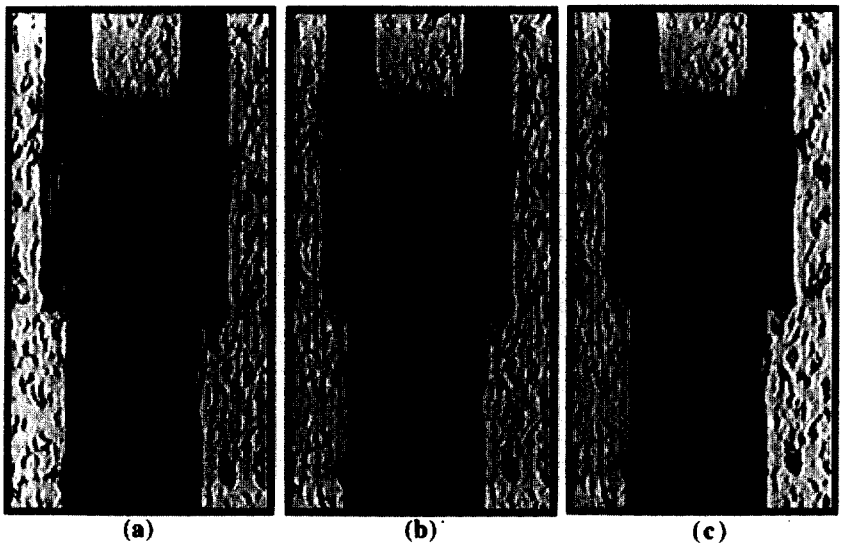

Fig. 8. Damage progression for the mini-shear test.

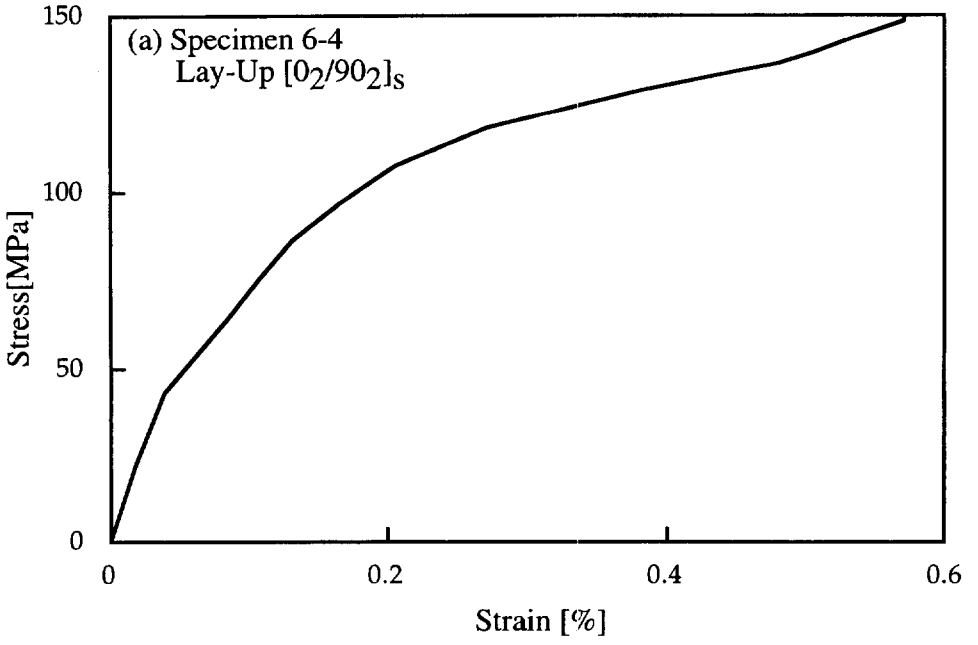

Fig. 5a. The response of a ceramic cross-ply laminate: stress–strain behavior.

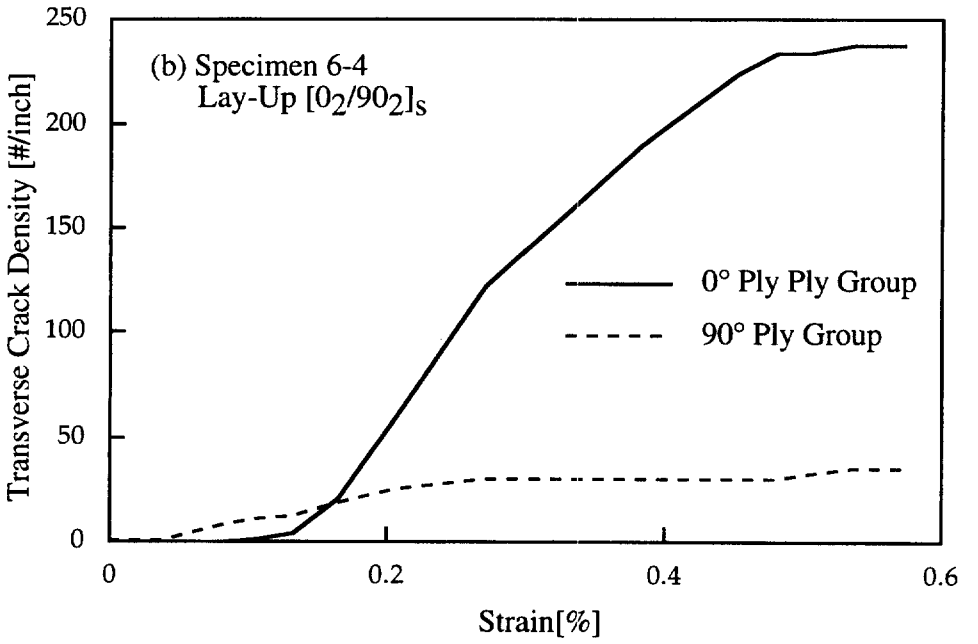

Fig. 5b. The response of a ceramic cross-ply laminate: crack density progression.

$$\tau_{xz}^{(i)} = C_{55}^{(i)} \frac{\partial u_i}{\partial z} \qquad i = 1, 2 \tag{3}$$

Employing the boundary and continuity conditions $\tau_{xz}^{(2)}(x, z_2 = h_2) = 0$, $\tau_{xz}^{(1)}(x, z_1 = 0) = 0$, $\tau_{xz}^{(1)}(x, z_1 = h_1) = \tau_{xz}^{(2)}(x, z_2 = 0) \equiv \tau^*(x)$ and $u_1(x, z_1 = h_1) = u_2(x, z_2 = 0)$ together with eqns (1) and (3) it is possible to express the shearing stresses in terms of the average displacements as follows:

Table 1. Cross-ply strength and damage data

Spec. No.	Lay-up	σ_{ult} [MPa]	$\sigma_{initiation}$ [MPa] 90° plies	$\sigma_{initiation}$ [MPa] 0° plies	Saturation density [#/in] 90° plies	Saturation density [#/in] 0° plies
6-1	$[0_2/90_2]_s$	151.0	65	65	32	180
6-2	$[0_2/90_2]_s$	145.8	103	86	20	122
6-3	$[0_2/90_2]_s$	136.9	48	108	36	146
6-4	$[0_2/90_2]_s$	151.9	65	76	34	238
6-5	$[0_2/90_2]_s$	154.9	42	105	40	180
6-6*	$[0_2/90_2]_s$	139.0	NA	NA	NA	NA
6-7*	$[0_2/90_2]_s$	139.3	NA	NA	NA	NA
6-8*	$[0_2/90_2]_s$	149.0	NA	NA	NA	NA
5-3	$[0_2/90_4]_s$	134.7	72	50	20	186
5-4	$[0_2/90_4]_s$	136.6	51	51	24	192

* Continuous loading tests.

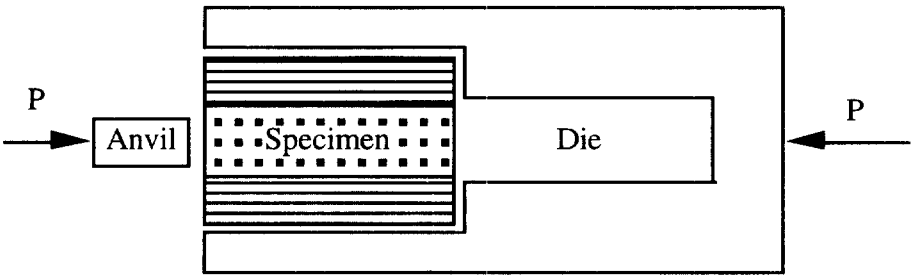

Fig. 6. Mini-shear inter-ply strength fixture.

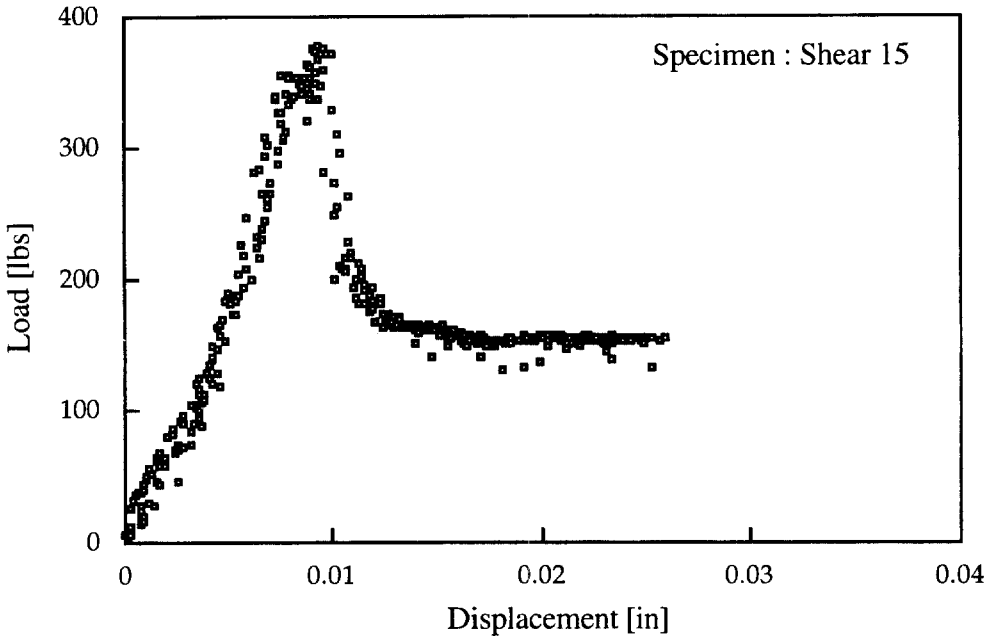

Fig. 7. Typical load displacement response of the mini-shear specimen.

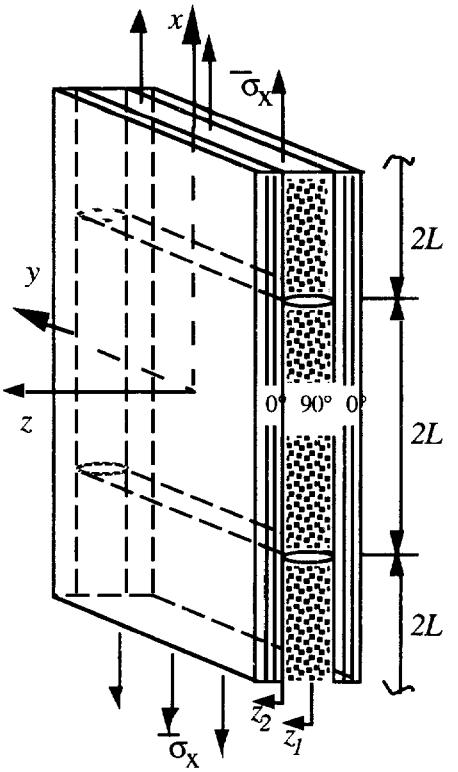

Fig. 9. Cross-ply specimen geometry.

$$\tau_{xz}^{(i)} = \frac{3C_{55}^{(1)}C_{55}^{(2)}}{C_{55}^{(1)}h_2 + C_{55}^{(2)}h_1}\frac{\bar{u}_2 - \bar{u}_1}{h_1}z_1$$

$$\tau_{xz}^{(2)} = \frac{3C_{55}^{(1)}C_{55}^{(2)}}{C_{55}^{(1)}h_2 + C_{55}^{(2)}h_1}\frac{\bar{u}_2 - \bar{u}_1}{h_2}(h_2 - z_2) \tag{4}$$

Note that these expressions are equivalent to those adopted in earlier articles (e.g., Nuismer and Tan, 1988, 1989; Lee and Daniel, 1990).

In particular, the interfacial shearing stress becomes:

$$\tau^* = A_{55}\left(\frac{\bar{u}_2 - \bar{u}_1}{\bar{h}}\right) \qquad \text{where } A_{55} = \frac{3\bar{h}C_{55}^{(1)}C_{55}^{(2)}}{h_1C_{55}^{(2)} + h_2C_{55}^{(1)}} \tag{5}$$

Where the "overbar" indicates an average with respect to z, namely:

$$\bar{f}_i(x) = \frac{1}{h_i}\int_0^{h_i} f(x, z_i)\,\mathrm{d}z_i \tag{6}$$

Additionally, we employ primes to denote differentiation with respect to x.

Turning to the normal (axial) stresses, from lamination theory we have:

$$\bar{\sigma}_x^{(i)} = Q_{11}^{(i)}\bar{u}_i' + Q_{12}^{(i)}\bar{\varepsilon}_y$$

$$\bar{\sigma}_y^{(i)} = Q_{12}^{(i)}\bar{u}_i' + Q_{22}^{(i)}\bar{\varepsilon}_y \tag{7}$$

In addition, the force balance relations read:

$$\bar{\sigma}_x'^{(1)} = -\frac{\tau^*(x)}{h_1}$$

$$\bar{\sigma}_x'^{(2)} = \frac{\tau^*(x)}{h_2} \tag{8}$$

which, upon integration with respect to x yield the "global" equilibrium expression:

$$\bar{\sigma}_x^{(1)} h_1 + \bar{\sigma}_x^{(2)} h_2 = \bar{\sigma}_x \bar{h} \tag{9}$$

where $\bar{\sigma}_x$ is the average applied far-field stress. Differentiation of eqns (7) with respect to x, substitution into eqns (8) and employment of eqn (5) yield:

$$\tau''^* - \alpha_0^2 \tau^* = 0 \qquad \text{where } \alpha_0^2 = \frac{A_{55}}{\bar{h}} \left(\frac{1}{h_1 Q_{11}^{(1)}} + \frac{1}{h_2 Q_{11}^{(2)}} \right) \tag{10}$$

The general solution of (10), $\tau^*(x) = A_0 \sinh(\alpha_0 x) + B_0 \cosh(\alpha_0 x)$ reduces to

$$\tau^*(x) = A_0 \sinh(\alpha_0 x) \tag{11}$$

since by symmetry we have $\tau^*(x = 0) = 0$. Furthermore, the traction free crack surface at $x = L$ implies:

$$\bar{\sigma}_x^{(1)}(x = L) = 0 \tag{12}$$

which in view of (9) gives

$$\bar{\sigma}_x^{(2)}(x = L) = \frac{\bar{\sigma}_x \bar{h}}{h_2} \tag{13}$$

To determine A_0 in eqn (11), we equate $\tau'^*(L)$ between eqn (5) and (11) and utilize eqns (12) and (14) to represent $\bar{u}_1'(L)$ and $\bar{u}_2'(L)$ in the first of eqns (7) in terms of $\bar{\sigma}_x$. We then obtain:

$$A_0 = \frac{\tau'^*(L)}{\alpha_0 \cosh(\alpha_0 L)} \tag{14}$$

where

$$\tau'^*(L) = \frac{A_{55}}{\bar{h} Q_{11}^{(1)}} \left(\frac{\bar{\sigma}_x \bar{h} Q_{11}^{(1)}}{h_2 Q_{11}^{(2)}} + \bar{\varepsilon}_y \left(Q_{12}^{(1)} - \frac{Q_{12}^{(2)}}{Q_{11}^{(2)}} Q_{11}^{(1)} \right) \right)$$

The expression for $\bar{\varepsilon}_y$ is derived from the condition of transverse equilibrium. In the absence of loading in the y-direction we have:

$$\bar{\sigma}_y \bar{h} L = h_1 \int_0^L \bar{\sigma}_y^{(1)} \, \mathrm{d}x + h_2 \int_0^L \bar{\sigma}_y^{(2)} \, \mathrm{d}x = 0 \tag{15}$$

The detailed expression for $\bar{\varepsilon}_y$ is given in eqn (A1) of the Appendix.

In summary, the stress distributions are given by:

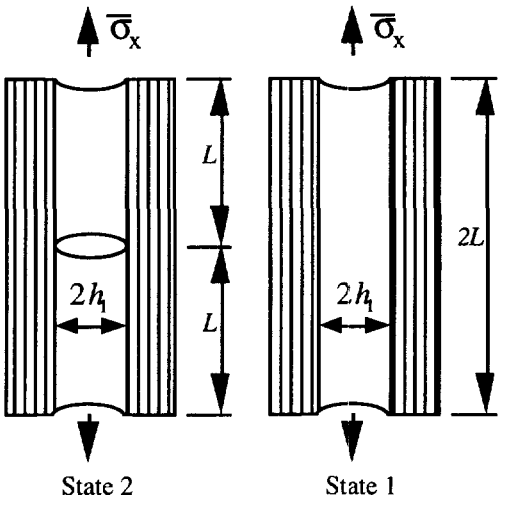

Fig. 10a. Progression of transverse matrix cracks (edge view).

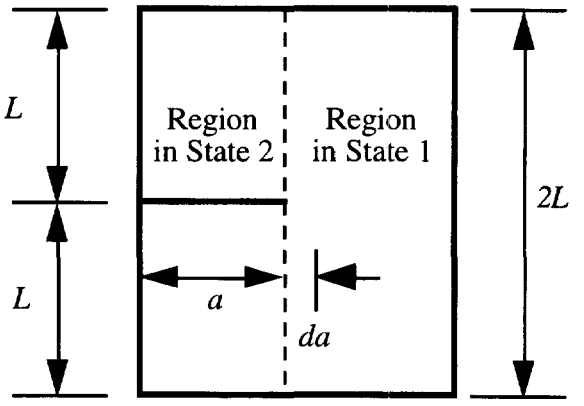

Fig. 10b. Progression of transverse matrix cracks (side view).

$$\tau^*(x) = A_0 \sinh(\alpha_0 x)$$

$$\bar{\sigma}_x^{(1)}(x) = \frac{A_0}{h_1 \alpha_0}(\cosh(\alpha_0 L) - \cosh(\alpha_0 x))$$

$$\bar{\sigma}_x^{(2)}(x) = \frac{\bar{\sigma}_x \bar{h}}{h_2} - \frac{\bar{\sigma}_x^{(1)}(x) h_1}{h_2}$$

$$\tau_{xz}^{(1)}(x, z_1) = \tau^*(x) z_1 / h_1, \qquad \tau_{xz}^{(2)}(x, z_2) = \tau^*(x) \frac{h_2 - z_2}{h_2} \tag{16}$$

Since the outer, 0° plies remain intact, straightforward integration of eqn (7) yields the average axial strain:

$$\bar{\varepsilon}_x = \frac{\bar{u}_2(L)}{L} = \frac{1}{Q_{11}^{(2)}} \left(\frac{\bar{\sigma}_x \bar{h}}{h_2} - Q_{12}^{(2)} \bar{\varepsilon}_y - \frac{A_0}{h_2 \alpha_0} \left(\cosh(\alpha_0 L) - \frac{\sinh(\alpha_0 L)}{\alpha_0 L} \right) \right) \tag{17}$$

To correlate the crack spacing, $2L$ with the applied stress $\bar{\sigma}_x$, we employ a fracture criterion and assume that new cracks will form midway between existing cracks whenever the available energy equals the energy required for new crack formation.

For that purpose, consider a steady-state transition between crack geometry states "1" and "2", with associated crack spacings of $2L$ and L, respectively, as depicted in Fig. 10(a).

We assume that as cracks progress in the 90° ply group, they span the thickness, $2h_1$. The energy available for crack growth, J, is given by Anderson (1991):

$$J = -\frac{d\Pi}{dA} \qquad \text{with } \Pi = U - W = -U^* \tag{18}$$

In eqn (18) Π is the total potential energy of the system, U is the elastic strain energy, W is the external work done on the system, and U^* is the complementary energy, while $dA = 2h_1\,da$ denotes the new fracture surface area. Consequently $J = (1/2h_1)(dU^*/da)$ which, in view of the assumption of steady state crack propagation, yields $J = (1/2h_1)$ [$2U^*$ (state "2") $- U^*$ (state "1")]. The foregoing result is expressed as:

$$J = \frac{2U^*|_{L/2} - U^*|_L}{2h_1} \tag{19}$$

The criterion for new crack formation is given by:

$$J = J_c \tag{20}$$

where J_c, the critical value, is a material property that can be determined experimentally for a given material system.

The complementary energy contains both the normal and shearing stress components. For state "1", with a crack spacing of $2L$ we have:

$$U^*|_L = 4h_1 \int_0^L \int_0^{\sigma_x^{(1)}} \tilde{\varepsilon}_x^{(1)}(\tilde{\sigma}_x^{(1)})\,d\tilde{\sigma}_x^{(1)}\,dx + 4h_2 \int_0^L \int_0^{\sigma_x^{(2)}} \tilde{\varepsilon}_x^{(2)}(\tilde{\sigma}_x^{(2)})\,d\tilde{\sigma}_x^{(2)}\,dx$$
$$+4\int_0^L \int_0^{h_1} \int_0^{\tau_{xz}^{(1)}} \tilde{\gamma}_{xz}^{(1)}(\tau_{xz}^{(1)})\,d\tilde{\tau}_{xz}^{(1)}\,dz\,dx + 4\int_0^L \int_{h_1}^{h} \int_0^{\tau_{xz}^{(2)}} \tilde{\gamma}_{xz}^{(2)}(\tilde{\tau}_{xz}^{(2)})\,d\tilde{\tau}_{xz}^{(2)}\,dz\,dx \tag{21}$$†

An analogous expression for $U^*|_{L/2}$ can also be obtained by adjusting the limits of integration. However, it should be noted that the integrands in (21) will depend on the crack spacing L. For instance, straightforward evaluation of the last two integrals in (21) yields the closed-form expression for the complementary energy due to shearing stresses:

$$U_\tau^* = \frac{2A_0^2}{3}\left(\frac{\sinh(2\alpha_0 L)}{4\alpha_0} - \frac{L}{2}\right)\left(\frac{h_1}{C_{55}^{(1)}} + \frac{h_2}{C_{55}^{(2)}}\right)$$

A correlation between crack spacing L and levels of applied stress $\bar{\sigma}_x$ is obtained by incrementing $\bar{\sigma}_x$ gradually, and evaluating the available energy J at each stress level for comparison with J_c. A new crack configuration (crack spacings are halved) occurs when $J = J_c$. At this stage comparisons of energies levels are made between $U^*|_{L/2}$ and $U^*|_{L/4}$ and so on. The stress–strain relation is obtained from (17), however since the applied stress $\bar{\sigma}_x$ is assumed to remain constant when $J = J_c$, there is a corresponding jump in strain $\bar{\varepsilon}_x$.

† Clearly, in the linear case $U^* = U$ and the integral in eqn (21) can be converted to surface integrals resulting in obvious simplifications. However, our main purpose here is to lay the groundwork for the non-linear response of the 0° ply groups where U^* and U are not equal.

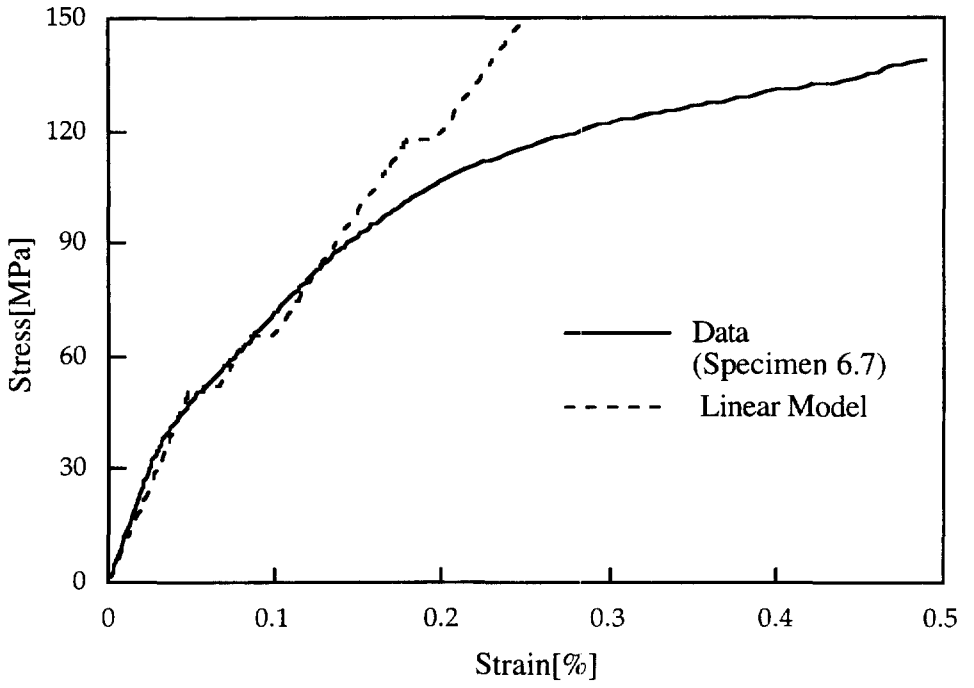

Fig. 11. Comparison of linear model and experimental stress–strain response.

A typical comparison between data and predictions that assume linear material behavior are shown in Fig. 11. We note an unacceptable discrepancy between the two curves when $\bar{\sigma}_x$ exceeds 90 MPa.

3.2. *Non-linear response of the* 0° *ply group*

The stress–strain response of the 0° plies exhibits pronounced non-linearity as shown in Fig. 2. This non-linear behavior is due to the formation of matrix cracks bridged by intact fibers, which is accompanied by interfacial fiber/matrix slippage. At higher stress levels, after matrix cracking has attained saturation density, additional damage is caused by fiber fragmentation and pull-outs.

To simplify the ensuing analysis the stress–strain response of the 0° plies will be represented by the bilinear curve depicted by the solid line in Fig. 12, with a "knee" at $\bar{\sigma}_x = \sigma_0 = 200$ MPa and stiffnesses $Q_{11}^{(2)}$ and $\tilde{Q}_{11}^{(2)}$ below and above σ_0. Consequently, eqns (7) are replaced by

$$\begin{aligned} \bar{\sigma}_x^{(i)} &= Q_{11}^{(i)}\bar{u}_i' + Q_{12}^{(i)}\bar{\varepsilon}_y \\ \bar{\sigma}_y^{(i)} &= Q_{12}^{(i)}\bar{u}_i' + Q_{22}^{(i)}\bar{\varepsilon}_y \end{aligned} \qquad i = 1, 2 \tag{22}$$

while

$$\begin{aligned} \bar{\sigma}_x^{(2)} &= Q_{11}^{(2)}\bar{u}_2' + Q_{12}^{(2)}\bar{\varepsilon}_y \qquad (\bar{\sigma}_x^{(2)} \leqslant \sigma_0) \\ \bar{\sigma}_x^{(2)} &= \tilde{Q}_{11}^{(2)}\bar{u}_2' + Q_{12}^{(2)}\bar{\varepsilon}_y + \hat{\sigma} \qquad (\bar{\sigma}_x^{(2)} < \sigma_0) \end{aligned} \tag{23}$$

with

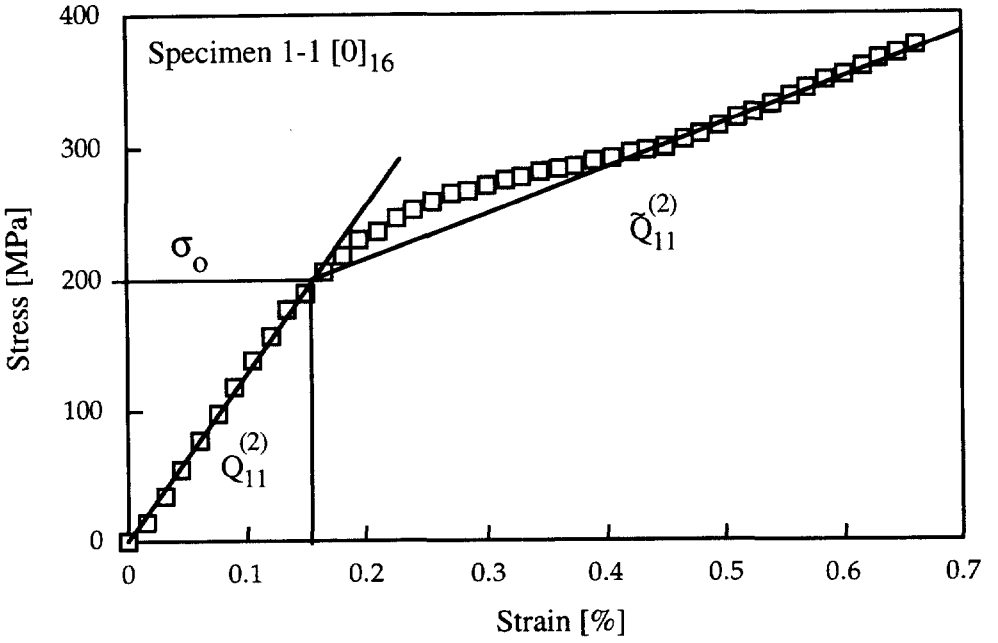

Fig. 12. Bilinear representation of the unidirectional stress–strain curve.

$$\hat{\sigma} = \sigma_0 \left(1 - \frac{\tilde{Q}_{11}^{(2)}}{Q_{11}^{(2)}}\right)$$

Since $\bar{\sigma}_x^{(2)}$ attains its maximal value at $x = L$, where $\bar{\sigma}_x^{(2)} = \bar{\sigma}_x \bar{h}/h_2$, it is clear that a non-linear region will emanate from $x = L$ towards $x = 0$ for $\bar{\sigma}_x \geqslant \sigma_0 \bar{h}/h_2$. When $\bar{\sigma}_x < \sigma_0 \bar{h}/h_2$ linear response will prevail within the entire region $0 \leqslant x \leqslant L$, while if $\bar{\sigma}_x^{(2)}(x = 0) \geqslant \sigma_0$ the 0° plies will respond non-linearly over the entire domain.

In general, non-linear response of the 0° plies will occur for $x^* \leqslant x \leqslant L$ while linear response is confined to $0 \leqslant x < x^*$, and by definition:

$$\bar{\sigma}_x^{(2)}(x^*) = \sigma_0 \tag{24}$$

Consequently, eqns (22) hold for $0 \leqslant x \leqslant L$ while the first and second eqns of (23) are valid for $0 \leqslant x < x^*$ and $x^* \leqslant x \leqslant L$, respectively.

The formulation of the present circumstance resembles that of the preceding subsection, but requires several modifications. Expression (10) and its solution given in (11) remain valid for $0 \leqslant x < x^*$, while over the remaining range we have:

$$\tau''^* - \alpha_1^2 \tau^* = 0, \qquad \alpha_1^2 = \frac{A_{55}}{\bar{h}} \left(\frac{1}{h_1 Q_{11}^{(1)}} + \frac{1}{h_2 \tilde{Q}_{11}^{(2)}}\right) \qquad (x^* \leqslant x \leqslant L) \tag{25}$$

whose solution is:

$$\tau^*(x) = A_1 \sinh(\alpha_1 x) + B_1 \cosh(\alpha_1 x) \tag{26}$$

The three unknowns A_1, B_1 and x^* can be evaluated with the aid of boundary conditions in (24) and the continuity requirements:

$$\tau^*(x^*+) = \tau^*(x^*-)$$
$$\bar{\sigma}_x^{(2)}(x^*+) = \bar{\sigma}_x^{(2)}(x^*-) \tag{27}$$

The expressions for A_1, B_1 and $\bar{\varepsilon}_y$ [the latter determined employing (15)] are given in the Appendix, eqns (A2) and (A3). These expressions contain the yet undetermined value of x^*, which is obtained through numerical iteration until the condition in (24) is satisfied. The stress field is expressed as follows:

$$\begin{aligned}
\tau^*(x) &= A_0 \sinh(\alpha_0 x) \\
\bar{\sigma}_x^{(1)} &= \frac{\bar{\sigma}_x \bar{h}}{h_1} - \frac{\sigma_0 h_2}{h_1} + \frac{A_0}{h_1 \alpha_0}(\cosh(\alpha_0 x^*) - \cosh(\alpha_0 x)) \qquad (0 \leqslant x < x^*) \\
\bar{\sigma}_x^{(2)} &= \frac{\bar{\sigma}_x \bar{h}}{h_2} - \frac{\bar{\sigma}_x^{(1)} h_1}{h_2}
\end{aligned} \tag{28}$$

while

$$\begin{aligned}
\tau^*(x) &= A_1 \sinh(\alpha_1 x) + B_1 \cosh(\alpha_1 x) \\
\bar{\sigma}_x^{(1)} &= \frac{1}{h_1 \alpha_1} \left\{ \begin{matrix} A_1(\cosh(\alpha_1 L) - \cosh(\alpha_1 x)) \\ + B_1(\sinh(\alpha_1 L) - \sinh(\alpha_1 x)) \end{matrix} \right\} \qquad (x^* \leqslant x < L) \\
\bar{\sigma}_x^{(2)} &= \frac{\bar{\sigma}_x \bar{h}}{h_2} - \frac{\bar{\sigma}_x^{(1)} h_1}{h_2}
\end{aligned} \tag{29}$$

The average global strain is again determined according to the same procedure as the previous sub-section. Upon integration of the constitutive relation for the 0° plies we get:

$$\begin{aligned}
\bar{\varepsilon}_x = \frac{1}{Q_{11}^{(2)} L} &\left\{ \sigma_0 x^* - \frac{A_0}{h_2 \alpha_0}(x^* \cosh(\alpha_0 x^*) - \sinh(\alpha_0 x^*)/\alpha_0) - Q_{12}^{(2)} \bar{\varepsilon}_y x^* \right\} + \frac{1}{\tilde{Q}_{11}^{(2)} L} \\
&\times \left\{ \begin{matrix} \dfrac{\bar{\sigma}_x \bar{h}(L - x^*)}{h_2} - \dfrac{1}{h_2 \alpha_1} \left[\begin{matrix} A_1((L - x^*)\cosh(\alpha_1 L) - \sinh(\alpha_1 L)/\alpha_1 + \sinh(\alpha_1 x^*)/\alpha_1) \\ + B_1((L - x^*)\sinh(\alpha_1 L) - \cosh(\alpha_1 L)/\alpha_1 + \cosh(\alpha_1 x^*)/\alpha_1) \end{matrix} \right] \\ - (Q_{12}^{(2)} \bar{\varepsilon}_y + \hat{\sigma})(L - x^*) \end{matrix} \right\}
\end{aligned} \tag{30}$$

The circumstance that $\bar{\sigma}_x^{(2)}(x = 0) \geqslant \sigma_0$ yields the simpler results:

$$\begin{aligned}
\tau^*(x) &= A_1 \sinh(\alpha_1 x) \\
\bar{\sigma}_x^{(1)}(x) &= \frac{A_1}{h_1 \alpha_1}(\cosh(\alpha_1 L) - \cosh(\alpha_1 x)) \\
\bar{\sigma}_x^{(2)}(x) &= \frac{\bar{\sigma}_x \bar{h} - \bar{\sigma}_x^{(1)} h_1}{h_2}
\end{aligned} \tag{31}$$

with

$$\bar{\varepsilon}_x = \frac{\bar{u}_2(L)}{L} = \frac{1}{\tilde{Q}_{11}^{(2)}} \left\{ \frac{\bar{\sigma}_x \bar{h}}{h_2} - \frac{A_1}{h_2 \alpha_1} \left(\cosh(\alpha_1 L) - \frac{\sinh(\alpha_1 L)}{\alpha_1 L} \right) - (Q_{12}^{(2)} \bar{\varepsilon}_y + \hat{\sigma}) \right\} \tag{32}$$

Note that the expressions for the shearing stresses $\tau_{xz}^{(1)}$ and $\tau_{xz}^{(2)}$ with z retain the forms listed in (16).

The prediction of crack spacing and density, which follows the reasoning expressed in eqns (18)–(20), requires the evaluation of the complementary energy U^*. In the present case, the integrations with respect to x must be split between the range $0 \leqslant x < x^*$, which is governed by eqns (28) and the first of (23), and the range $x^* \leqslant x < L$ where eqns (29) and (23) apply [eqns (22) apply to both regions]. Consequently, over the range $x^* \leqslant x < L$

the inner integration with respect to $\bar{\sigma}_x^{(2)}$ must be further divided between the ranges $0 \leqslant \bar{\sigma}_x^{(2)} \leqslant \sigma_0$ and $\sigma_0 \leqslant \bar{\sigma}_x^{(2)} \leqslant \bar{\sigma}_x^{(2)}$. The resulting complementary energy is then given by:

$$U^*|_L = I_1 + I_2 + I_3 + I_4 \tag{33}$$

where

$$I_1 = \frac{4h_1}{Q_{11}^{(1)}}\left\{\int_0^{x^*}\left(\frac{(\bar{\sigma}_x^{(1)})^2}{2} - \bar{\sigma}_x^{(1)}Q_{12}^{(1)}\bar{\varepsilon}_y\right)\mathrm{d}x + \int_{x^*}^{L}\left(\frac{(\bar{\sigma}_x^{(1)})^2}{2} - \bar{\sigma}_x^{(1)}Q_{12}^{(1)}\bar{\varepsilon}_y\right)\mathrm{d}x\right\}$$

$$I_2 = \frac{4h_2}{Q_{11}^{(2)}}\int_0^{x^*}\left(\frac{(\bar{\sigma}_x^{(2)})^2}{2} - \bar{\sigma}_x^{(2)}\bar{\varepsilon}_y Q_{12}^{(2)}\right)\mathrm{d}x + \frac{4h_2}{\tilde{Q}_{11}^{(2)}}\int_{x^*}^{L}\left(\frac{(\bar{\sigma}_x^{(2)})^2}{2} - \bar{\sigma}_x^{(2)}(\bar{\varepsilon}_y Q_{12}^{(2)} + \hat{\sigma})\right)\mathrm{d}x$$
$$+ 4h_2(L - x^*)\left\{\frac{1}{Q_{11}^{(2)}}\left(\frac{\sigma_0^2}{2} - \sigma_0\bar{\varepsilon}_y Q_{12}^{(2)}\right) + \frac{1}{\tilde{Q}_{11}^{(2)}}\left(\sigma_0(\bar{\varepsilon}_y Q_{12}^{(2)} + \hat{\sigma}) - \frac{\sigma_0^2}{2}\right)\right\}$$

$$I_3 = \frac{2A_0^2}{3}\left(\frac{\sinh(2\alpha_0 x^*)}{4\alpha_0} - \frac{x^*}{2}\right)\left(\frac{h_1}{C_{55}^{(1)}} + \frac{h_2}{C_{55}^{(2)}}\right)$$

$$I_4 = \frac{2}{3}\left(\frac{h_1}{C_{55}^{(1)}} + \frac{h_2}{C_{55}^{(2)}}\right)\left\{\frac{(A_1^2 + B_1^2)}{4\alpha_1}[\sinh(2\alpha_1 L) - \sinh(2\alpha_1 x^*)]\right.$$
$$\left. + \frac{(B_1^2 - A_1^2)(L - x^*)}{2} + \frac{A_1 B_1}{2\alpha_1}[\cosh(2\alpha_1 L) - \cosh(2\alpha_1 x^*)]\right\}$$

The integrals I_1 and I_2 express the contributions of the normal stresses, while I_3 and I_4 account for the contributions of the shearing stresses $\tau_{xz}^{(i)}$ over the ranges $0 \leqslant x < x^*$ and $x^* \leqslant x < L$, respectively.

For the case when $\bar{\sigma}_x^{(2)}(x = 0) \geqslant \sigma_0$ the computation of U^* reduces to:

$$U^*|_L = \hat{I}_1 + \hat{I}_2 \tag{34}$$

with

$$\hat{I}_1 = \frac{4h_1}{Q_{11}^{(1)}}\int_0^{L}\left(\frac{(\bar{\sigma}_x^{(1)})^2}{2} - \bar{\sigma}_x^{(1)}\bar{\varepsilon}_y Q_{12}^{(1)}\right)\mathrm{d}x + \frac{4h_2}{\tilde{Q}_{11}^{(2)}}\int_0^{L}\left(\frac{(\bar{\sigma}_x^{(2)})^2}{2} - \bar{\sigma}_x^{(2)}(\bar{\varepsilon}_y Q_{12}^{(2)} + \hat{\sigma})\right)\mathrm{d}x$$
$$+ 4h_2 L\left\{\frac{\sigma_0^2}{2}\left(\frac{1}{Q_{11}^{(2)}} - \frac{1}{\tilde{Q}_{11}^{(2)}}\right) + \sigma_0\left(\frac{\bar{\varepsilon}_y Q_{12}^{(2)} + \hat{\sigma}}{\tilde{Q}_{11}^{(2)}} - \frac{\bar{\varepsilon}_y Q_{12}^{(2)}}{Q_{11}^{(2)}}\right)\right\}$$

and, which upon evaluation of the integrations yields:

$$\hat{I}_2 = \frac{2A_1^2}{3}\left(\frac{\sinh(2\alpha_1 L)}{4\alpha_1} - \frac{L}{2}\right)\left(\frac{h_1}{C_{55}^{(1)}} + \frac{h_2}{C_{55}^{(2)}}\right)$$

A typical prediction for the stress–strain response is shown in Fig. 13(a). Note the significant improvement over the linear model. However, the comparison of predicted and observed crack densities, shown in Fig. 13(b) shows that there still remains a serious deficiency in the bilinear analysis. The discrepancy between observed and predicted crack densities persists over a significant range of assumed J_c values, as shown in Figs 14 and 15 for two cross-ply lay-ups. This divergence remains in spite of the reasonable agreement between predicted and observed stress–strain curves.

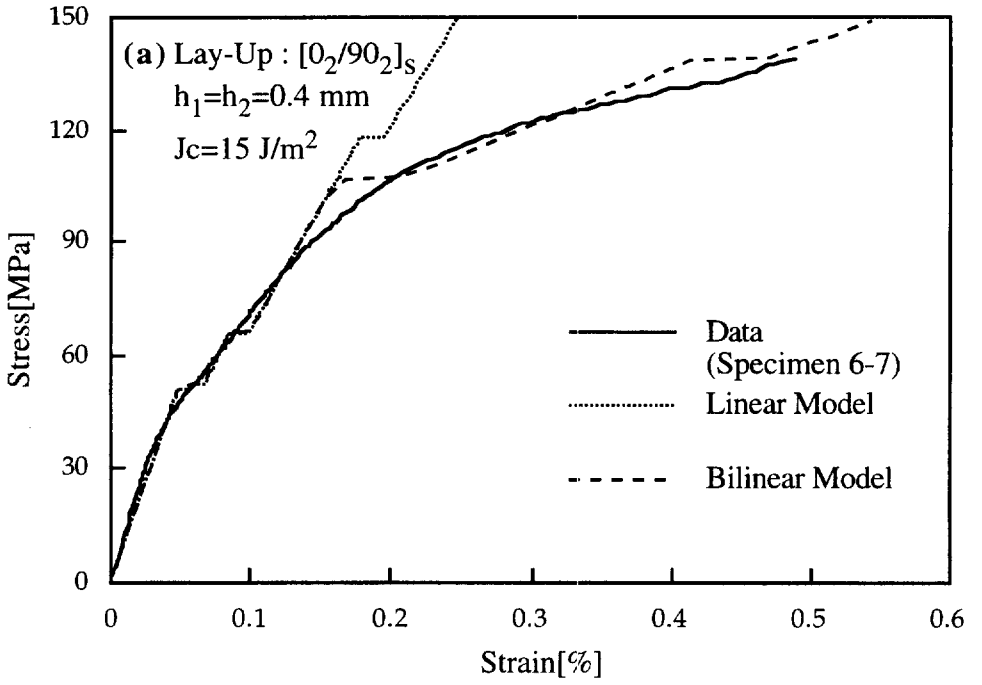

Fig. 13a. Comparison of bilinear and linear models with experimental stress–strain response.

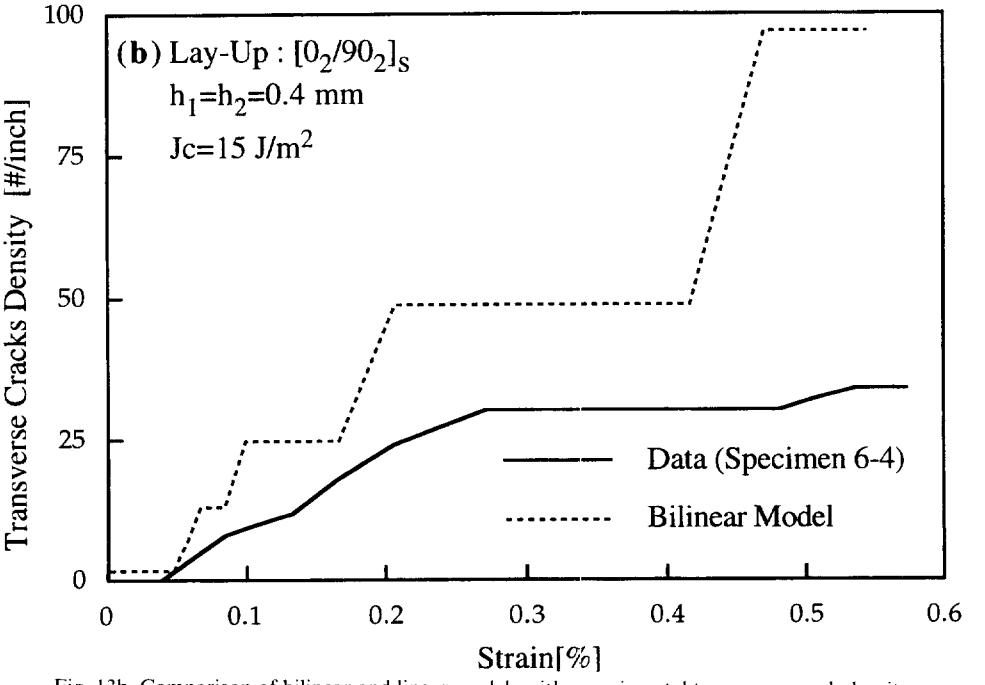

Fig. 13b. Comparison of bilinear and linear models with experimental transverse crack density.

3.3. *Non-linear response of the* 0° *ply groups with interlaminar slip*

As noted in Section 2, the 0/90° interface can support an interfacial shearing stress of finite magnitude, τ_s^*. Consequently, the analysis of Section 3.2 must be delimited by the

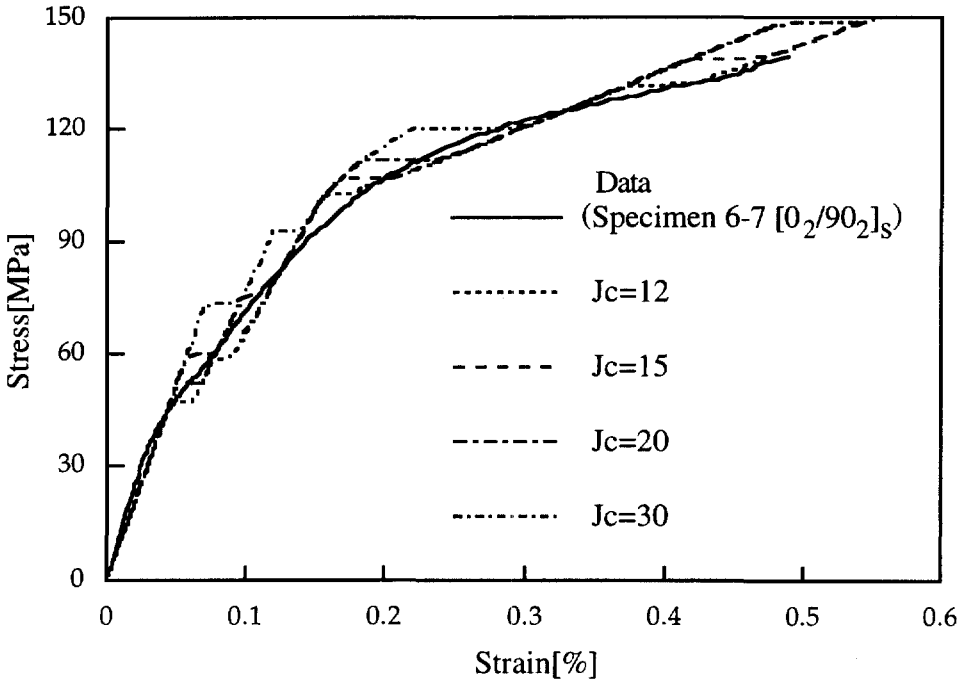

Fig. 14a. Effect of J_c [J/m^2] on the stress–strain response for a $[0_2/90_2]_s$ lay-up.

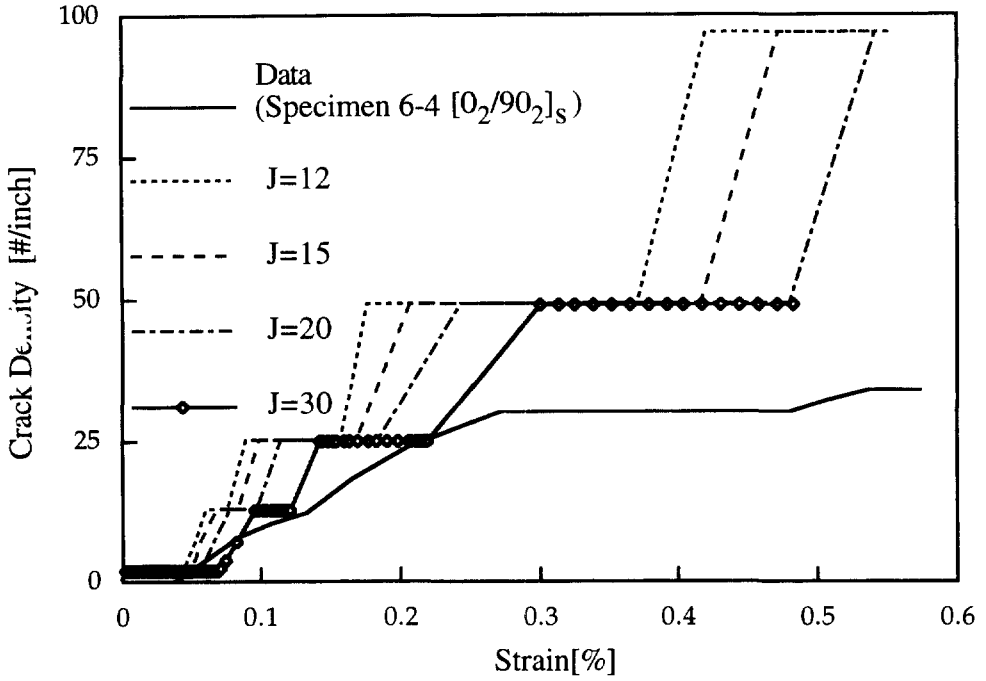

Fig. 14b. Effect of J_c [J/m^2] on transverse crack density for a $[0_2/90_2]_s$ lay-up.

restriction that $\tau^*(x) < \tau_s^*$. This restriction implies the existence of an interfacial slip region where $\tau^*(x) = \tau_s^*$.†

The results of Sub-sections 3.1 and 3.2 shows that $\tau^*(x)$ increases monotonically with x. Therefore, the condition $\tau^*(x) = \tau_s^*$ will occur first at $x = L$ and, upon further increase

† It should be noted that the shear-lag model cannot address coulomb friction since it incorporates the implicit assumption $\sigma_z \approx 0$, in view of the employment of laminate relations (7). These relations are analogous to those of classical plate theory.

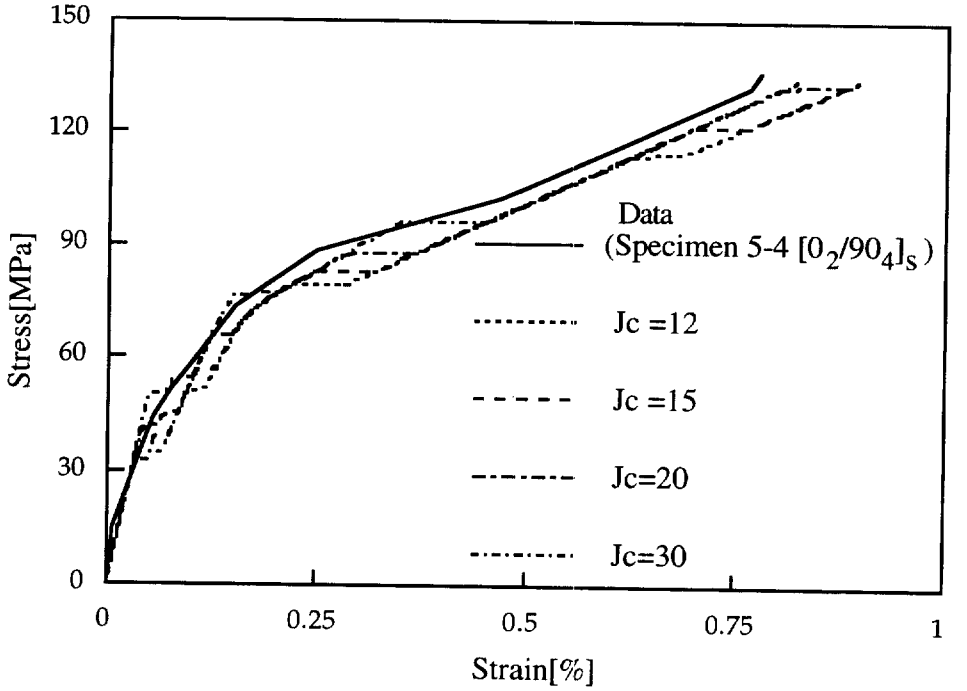

Fig. 15a. Effect of J_c [J/m^2] on the stress–strain response for a $[0_2/90_4]_s$ lay-up.

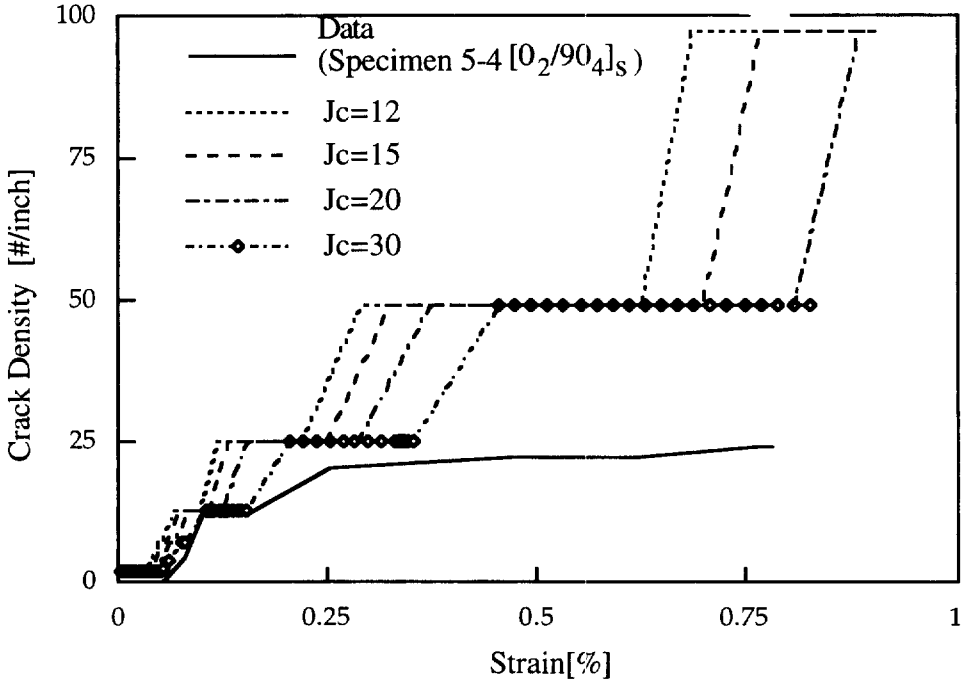

Fig. 15b. Effect of J_c [J/m^2] on transverse crack density for a $[0_2/90_4]_s$ lay-up.

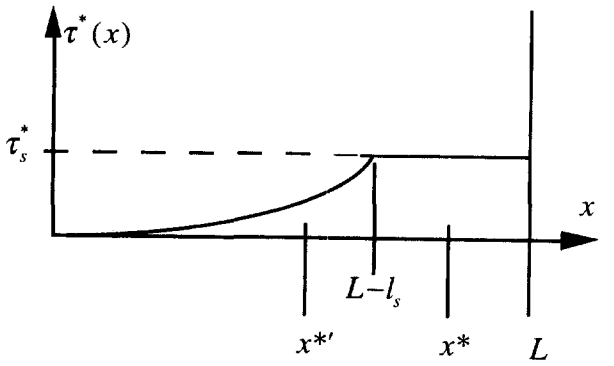

Fig. 16. Relative positions of the slip zone $L-l_s \leqslant x \leqslant L$ and the "knee point" x^*, $x^* \leqslant x \leqslant L$.

in $\bar{\sigma}_x$, will extend towards $x = 0$. Since τ_s^* and the "knee-point stress" σ_0 are independent material properties, the relative ranges of the interfacial slip zone and non-linear response of the 0° plies can vary with $\bar{\sigma}_x$ as depicted in Fig. 16. We distinguish between three cases:

"Case I": The slip zone encompasses the "yield" zone ($L-l_s < x^*$).
"Case II": The "yield" zone encompasses the slip zone ($L-l_s > x^*$).
"Case III": "Yielding" over the entire domain, i.e. $x^* = 0$, with slippage over the region $L-l_s \leqslant x \leqslant L$.

In all the above cases we have:

$$\tau^*(x) = \tau_s^* \qquad L-l_s \leqslant x \leqslant L \tag{35}$$

with the newly introduced unknown, l_s, which is determined from the condition:

$$\tau^*(x = L-l_s) = \tau_s^* \tag{36}$$

3.3.1. *Case I* ($x^* > L-l_s$) In view of (8), (12), (13) and (35) we have:

$$\begin{aligned} \tau^*(x) &= \tau_s^* \\ \bar{\sigma}_x^{(1)}(x) &= \frac{\tau_s^*(L-x)}{h_1} \qquad (x^* \leqslant x \leqslant L) \\ \bar{\sigma}_x^{(2)}(x) &= \frac{\bar{\sigma}_x \bar{h}}{h_2} - \frac{\tau_s^*(L-x)}{h_2} \end{aligned} \tag{37}$$

Together with eqn (24), the third of eqns (37) yields:

$$x^* = \frac{\sigma_0 h_2 - \bar{\sigma}_x \bar{h}}{\tau_s^*} + L \tag{38}$$

Within the adjacent slip region, eqns (8), (9), (24) and (35) give:

$$\begin{aligned} \tau^*(x) &= \tau_s^* \\ \bar{\sigma}_x^{(1)}(x) &= \frac{\tau_s^*(x^*-x)}{h_1} + \frac{\bar{\sigma}_x \bar{h} - \sigma_0 h_2}{h_1} \qquad (L-l_s \leqslant x < x^*) \end{aligned}$$

$$\bar{\sigma}_x^{(2)}(x) = \sigma_0 - \frac{\tau_s^* (x^* - x)}{h_2} \tag{39}$$

Substitution of (38) into (39) gives:

$$\bar{\sigma}_x^{(1)}(x = L - l_s) = \frac{\tau_s^* l_s}{h_1}$$

$$\bar{\sigma}_x^{(2)}(x = L - l_s) = \frac{\bar{\sigma}_x \bar{h}}{h_2} - \frac{\tau_s^* l_s}{h_2} \tag{40}$$

Note that the latter expressions can also be obtained from (8), (12), (13) and (35). Turning to the inner contact region, which is governed by linear response, the solution follows the format of Section 3.1, except that the boundary conditions (12) and (13) are replaced by those in eqns (40). We get:

$$\tau^*(x) = A_0 \sinh(\alpha_0 x)$$

$$\bar{\sigma}_x^{(1)}(x) = \frac{\tau_s^* l_s}{h_1} + \frac{A_0}{h_1 \alpha_0} \{\cosh(\alpha_0 (L - l_s)) - \cosh(\alpha_0 x)\} \qquad (0 \leqslant x < L - l_s)$$

$$\bar{\sigma}_x^{(2)}(x) = \frac{\bar{\sigma}_x \bar{h}}{h_2} - \frac{\bar{\sigma}_x^{(1)} h_1}{h_2} \tag{41}$$

where the expression for A_0 is given by eqn (A4) in the Appendix.

It should be noted that A_0 depends on l_s and $\bar{\varepsilon}_y$. The strain $\bar{\varepsilon}_y$, which is again determined through the use of (15), contains dependence on x^* (and l_s), since the integrations indicated in (15) involve expressions that vary within the subregions whose extent is defined by the location of x^*. Consequently, A_0 depends implicitly on x^* as well.

The solution for l_s can be obtained through numerical iteration as follows:

(1) Calculate x^* from eqn (38).
(2) Select a trial value for the slip zone length, l_s, consistent with $x^* > L - l_s$.
(3) Employing eqns (37), (39), (41), (7) and (15), evaluate $\bar{\varepsilon}_y$.
(4) Calculate A_0 from eqn (A4).
(5) Calculate τ^* $(x = L - l_s)$ using the first of eqns (41) and check to see if $\tau^*(x = L - l_s) = \tau_s^*$. If so, then l_s has been located. If not, it is necessary to perform another iteration by returning to step (1).

Finally, upon employing the appropriate forms for $\bar{\sigma}_x^{(2)}$ from (37), (39) and (41) the expression for the average axial strain becomes:

$$\bar{\varepsilon}_x = \frac{1}{L}\left[\int_0^{L-l_s} \frac{\bar{\sigma}_x^{(2)} - Q_{12}^{(2)} \bar{\varepsilon}_y}{Q_{11}^{(2)}} \mathrm{d}x + \int_{L-l_s}^{x^*} \frac{\bar{\sigma}_x^{(2)} - Q_{12}^{(2)} \bar{\varepsilon}_y}{Q_{11}^{(2)}} \mathrm{d}x + \int_{x^*}^{L} \frac{\bar{\sigma}_x^{(2)} - Q_{12}^{(2)} \bar{\varepsilon}_y - \hat{\sigma}}{\tilde{Q}_{11}^{(2)}} \mathrm{d}x\right] \tag{42}$$

3.3.2. *Case II* ($L - l_s > x^*$)

In this case linear response occurs in the inner region $0 \leqslant x < x^*$, where the stresses are given in forms whose appearance is identical to eqn (28), namely:

$$\tau^*(x) = A_0 \sinh(\alpha_0 x)$$

$$\bar{\sigma}_x^{(1)} = \frac{\bar{\sigma}_x \bar{h}}{h_1} - \frac{\sigma_0 h_2}{h_1} + \frac{A_0}{h_1 \alpha_0} (\cosh(\alpha_0 x^*) - \cosh(\alpha_0 x)) \qquad (0 \leqslant x < x^*)$$

$$\bar{\sigma}_x^{(2)} = \frac{\bar{\sigma}_x \bar{h}}{h_2} - \frac{\bar{\sigma}_x^{(1)} h_1}{h_2} \tag{43}$$

The outer region, $L-l_s \leqslant x \leqslant L$ is typified by the condition $\tau^*(x) = \tau_s^*$ which is associated with interlaminar slip (note that the non-linear stress–strain response of the 0° plies given in (23) applies). Consequently the expressions for the stresses coincide with eqns (37), namely:

$$\begin{aligned} \tau^*(x) &= \tau_s^* \\ \bar{\sigma}_x^{(1)}(x) &= \frac{\tau_s^*(L-x)}{h_1} \qquad (L-l_s \leqslant x \leqslant L) \\ \bar{\sigma}_x^{(2)}(x) &= \frac{\bar{\sigma}_x \bar{h}}{h_2} - \frac{\tau_s^*(L-x)}{h_2} \end{aligned} \tag{44}$$

At the edge of the slip zone eqns (45) give:

$$\begin{aligned} \bar{\sigma}_x^{(1)}(x = L-l_s) &= \frac{\tau_s^* l_s}{h_1} \\ \bar{\sigma}_x^{(2)}(x = L-l_s) &= \frac{\bar{\sigma}_x \bar{h}}{h_2} - \frac{\tau_s^* l_s}{h_2} \end{aligned} \tag{45}$$

The intermediate region, $x^* \leqslant x < L-l_s$, is characterized by non-linear response of the 0° plies, as expressed in (23), with a perfect bond at the 0/90° interface. The stress field in this region is similar to that in eqn (29), except that it must match the continuity of stresses at $x = L-l_s$ listed in (45). We have:

$$\begin{aligned} \tau^*(x) &= A_1 \sinh(\alpha_1 x) + B_1 \cosh(\alpha_1 x) \\ \bar{\sigma}_x^{(1)}(x) &= \frac{\tau_s^* l_s}{h_1} + \frac{1}{h_1 \alpha_1} \left\{ \begin{array}{l} A_1[\cosh(\alpha_1(L-l_s)) - \cosh(\alpha_1 x)] \\ + B_1[\sinh(\alpha_1(L-l_s)) - \sinh(\alpha_1 x)] \end{array} \right\} \qquad (x^* \leqslant x \leqslant L-l_s) \\ \bar{\sigma}_x^{(2)}(x) &= \frac{\bar{\sigma}_x \bar{h}}{h_2} - \frac{h_1 \bar{\sigma}_x^{(1)}(x)}{h_2} \end{aligned} \tag{46}$$

As in previous circumstances, the solution depends implicitly on $\bar{\varepsilon}_y$ through the stress–strain relations in (22) and (23). The transverse strain $\bar{\varepsilon}_y$ is again evaluated with the aid of eqn (15). However, for the present case integration over the region $0 \leqslant x \leqslant L$ must be subdivided over the intervals $0 \leqslant x < x^*$, $x^* \leqslant x < L-l_s$, and $L-l_s \leqslant x \leqslant L$, with appropriate expressions for $\bar{\sigma}_x^{(i)}$.

In the present case, the problem is fully coupled in x^* and l_s and the numerical solution involves a simultaneous iterative scheme. Expressions (43)–(46) contain the five unknowns A_0, A_1, B_1, x^* and l_s. These unknowns are uniquely determined upon employment of the boundary conditions in (12) and (13) as well as the continuity of $\tau^*(x)$ and $\bar{\sigma}_x^{(1)}$ at $x = x^*$ and $x = L-l_s$. Furthermore, by hypothesis, $\bar{\sigma}_x^{(2)}(x = x^*) = \sigma_0$ and $\tau^*(x = L-l_s) = \tau_s^*$. Detailed expressions for A_0, A_1, B_1, and $\bar{\varepsilon}_y$ are given by eqns (A5)–(A7) in the Appendix.

The average axial strain $\bar{\varepsilon}_x$ is given by:

$$\bar{\varepsilon}_x = \frac{1}{L}\left[\int_0^{x^*} \frac{\bar{\sigma}_x^{(2)} - Q_{12}^{(2)}\bar{\varepsilon}_y}{Q_{11}^{(2)}}\,dx + \int_{x^*}^{L-l_s} \frac{\bar{\sigma}_x^{(2)} - Q_{12}^{(2)}\bar{\varepsilon}_y - \hat{\sigma}}{\tilde{Q}_{11}^{(2)}}\,dx + \int_{L-l_s}^{L} \frac{\bar{\sigma}_x^{(2)} - Q_{12}^{(2)}\bar{\varepsilon}_y - \hat{\sigma}}{\tilde{Q}_{11}^{(2)}}\,dx\right] \tag{47}$$

3.3.3. *Case III* ($x^* = 0, 0 < l_s < L$)

In this case the stresses in the region $L-l_s \leqslant x \leqslant L$ are given by eqns (44) while within the inner region we have:

$$\tau^*(x) = A_0 \sinh(\alpha_1 x)$$

$$\bar{\sigma}_x^{(1)}(x) = \frac{\tau_s^* l_s}{h_1} + \frac{A_0}{h_1 \alpha_1}\{\cosh(\alpha_1(L-l_s)) - \cosh(\alpha_1 x)\} \qquad (0 \leqslant x < L-l_s)$$

$$\bar{\sigma}_x^{(2)}(x) = \frac{\bar{\sigma}_x \bar{h}}{h_2} - \frac{\bar{\sigma}_x^{(1)} h_1}{h_2} \tag{48}$$

The corresponding expressions for A_0 and $\bar{\varepsilon}_y$ are given in the Appendix, eqns (A8) and (A9). Also the expression for the average axial strain is:

$$\bar{\varepsilon}_x = \frac{1}{L}\int_0^{L-l_s} \frac{\bar{\sigma}_x^{(2)} - Q_{12}^{(2)}\bar{\varepsilon}_y - \hat{\sigma}}{\tilde{Q}_{11}^{(2)}}\,dx + \frac{1}{L}\int_{L-l_s}^{L} \frac{\bar{\sigma}_x^{(2)} - Q_{12}^{(2)}\bar{\varepsilon}_y - \hat{\sigma}}{\tilde{Q}_{11}^{(2)}}\,dx \tag{49}$$

3.3.4. *Complementary energies*

In Case I ($x^* > L-l_s$) the contributions of the normal stresses to $U^*|_L$ are given by the integrals I_1 and I_2 in eqn (33). However, due to the disparate expressions for $\bar{\sigma}_x^{(1)}$ and $\bar{\sigma}_x^{(2)}$ in (37) and (39) it is necessary to split integrations of I_1 and I_2 over the region $0 \leqslant x < x^*$ between the two segments $0 \leqslant x < L-l_s$ and $L-l_s \leqslant x \leqslant x^*$. On the other hand the contribution of the shearing stresses to $U^*|_L$ stems from the sub-regions $0 \leqslant x < L-l_s$ and $L-l_s \leqslant x \leqslant L$. This contribution is given by:

$$I_\tau^{(\mathrm{I})} = \frac{2}{3}\left\{A_0^2\left(\frac{\sinh(2\alpha_0(L-l_s))}{4\alpha_0} - \frac{L-l_s}{2}\right) + (\tau_s^*)^2 l_s\right\}\left\{\frac{h_1}{C_{55}^{(1)}} + \frac{h_2}{C_{55}^{(2)}}\right\} \tag{50}$$

In Case II ($x^* < L-l_s$) similar considerations apply to the contributions of the normal stresses, which are again given by I_1 and I_2 in eqn (33), except that in this case integrations over $x^* \leqslant x \leqslant L$ are divided among $x^* \leqslant x < L-l_s$ and $L-l_s \leqslant x \leqslant L$.

In this case the contribution of the shearing stress to $U^*|_L$ is given by:

$$I_\tau^{(\mathrm{II})} = \frac{2}{3}\left\{\begin{aligned} &A_0^2\left(\frac{\sinh(2\alpha_0(L-l_s))}{4\alpha_0} - \frac{x^*}{2}\right) + \frac{(A_1^2+B_1^2)}{4\alpha_1}\begin{bmatrix}\sinh(2\alpha_1(L-l_s)) \\ -\sinh(2\alpha_1 x^*)\end{bmatrix} \\ &+ \frac{(B_1^2-A_1^2)(L-l_s-x^*)}{2} + \frac{A_1 B_1}{2\alpha_1}\begin{bmatrix}\cosh(2\alpha_1(L-l_s)) \\ -\cosh(2\alpha_1 x^*)\end{bmatrix} + (\tau_s^*)^2 l_s\end{aligned}\right\} \times \left\{\frac{h_1}{C_{55}^{(1)}} + \frac{h_2}{C_{55}^{(2)}}\right\} \tag{51}$$

Finally, for Case III ($x^* = 0$), the complementary energy calculation is similar to Case I. However, it is necessary to replace x^* with $L-l_s$ in the limit of integration, while I_2 is replaced by:

$$\tilde{I}_2 = \frac{4h_2}{\tilde{Q}_{11}^{(2)}}\int_0^{L-l_s}\left(\frac{(\bar{\sigma}_x^{(2)})^2}{2} - \bar{\sigma}_x^{(2)}(\bar{\varepsilon}_y Q_{12}^{(2)} + \hat{\sigma})\right)dx + \frac{4h_2}{\tilde{Q}_{11}^{(2)}}\int_{L-l_s}^{L}\left(\frac{(\bar{\sigma}_x^{(2)})^2}{2} - \bar{\sigma}_x^{(2)}(\bar{\varepsilon}_y Q_{12}^{(2)} + \hat{\sigma})\right)dx$$
$$+ 4h_2 L\left\{\frac{\sigma_0^2}{2}\left(\frac{1}{Q_{11}^{(2)}} - \frac{1}{\tilde{Q}_{11}^{(2)}}\right) + \sigma_0\left(\frac{\bar{\varepsilon}_y Q_{12}^{(2)} + \hat{\sigma}}{\tilde{Q}_{11}^{(2)}} - \frac{\bar{\varepsilon}_y Q_{12}^{(2)}}{Q_{11}^{(2)}}\right)\right\} \tag{52}$$

Then the contribution of the shearing stress to $U^*|_L$ is given by:

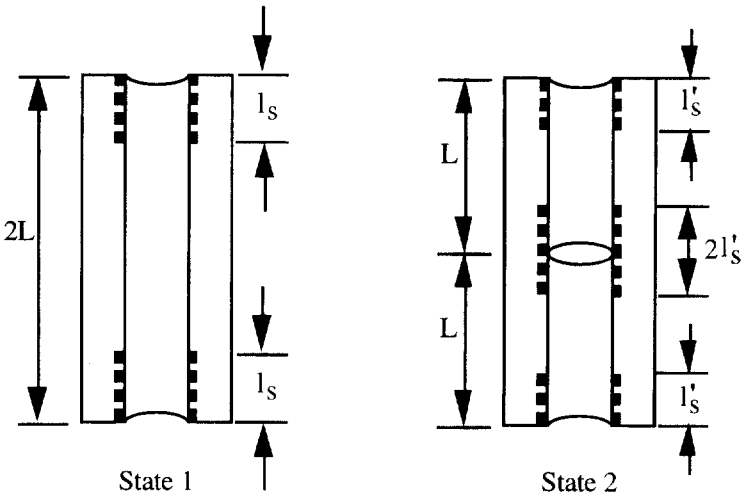

Fig. 17. The circumstances of $l'_s < l_s$.

$$U_\tau^* = \frac{2}{3}\left\{A_0^2\left(\frac{\sinh(2\alpha_1(L-l_s))}{4\alpha_1} - \frac{L-l_s}{2}\right) + (\tau_s^*)^2 l_s\right\}\left\{\frac{h_1}{C_{55}^{(1)}} + \frac{h_2}{C_{55}^{(2)}}\right\} \tag{53}$$

3.4. *Special considerations concerning the evolution of slip zones*

In some circumstances it may occur that a transition from "state 1" to "state 2", which involves the creation of new cracks centered between existing cracks, will be associated with new adjacent slip zones in length l'_s which turn out to be shorter than the length l_s associated with "state 1". Since the present analysis assumes symmetry about the mid-plane between neighboring cracks, $l'_s < l_s$ implies that reverse slip occurs near the "state 1" cracks in a scenario of monotonically increasing external loads. For obvious reasons such an event cannot occur in reality. This circumstance is depicted in Fig. 17.

Although $l'_s < l_s$ may indeed be feasible, it would be associated with interfacial "locking" over the range $l'_s < x < l_s$ rather than with reverse slip. However, stick-slip regions adjacent to some cracks and slip regions adjoining other cracks to not conform with the symmetry assumptions of the present analysis. In fact, any attempt to account for the sequential evolution of stick and slip regions near "older" and "newer" cracks will quickly become intractable.

To overcome the foregoing difficulty, we chose to set $l'_s = l_s$ whenever the analysis yielded $l'_s < l_s$. This implies that at the stress level corresponding to the transition from "state 1" to "state 2", as well as for some stresses exceeding that level, the length of the slip zone, l_s is no longer unknown and is taken as a prescribed quantity.

The analysis, which corresponds to three foregoing cases, I, II, III, involve simplified versions of the results presented in eqns (35)–(53). The full details are given by Erdman (1995).

4. PARAMETRIC STUDIES AND MODEL PREDICTIONS

Computations were performed for both $[0_2/90_2]_s$ and $[0_2/90_4]_s$ lay-ups with $J_c = 12$, 15, 20 and 30 J/m^2 and $\tau_s^* = 35$, 45 and 55 MPa, for a total of 24 case studies. Predicted stress–strain response and crack densities were compared with experimental data and observations. For the sake of brevity we focus attention to $J_c = 12$ and 15 J/m^2 over the foregoing range of τ_s^*. Results are shown in Figs 18–21. It is apparent that the closest agreement between model predictions and experimental data occurs for $J_c \sim 15$ J/m^2 and $\tau_s^* \sim 50$ MPa. The predictions associated with $J_c = 20$ and 30 J/m^2 fall above the experimental stress–strain curve and below the observed crack density data. Complete details are given in an earlier quoted work (Erdman, 1995).

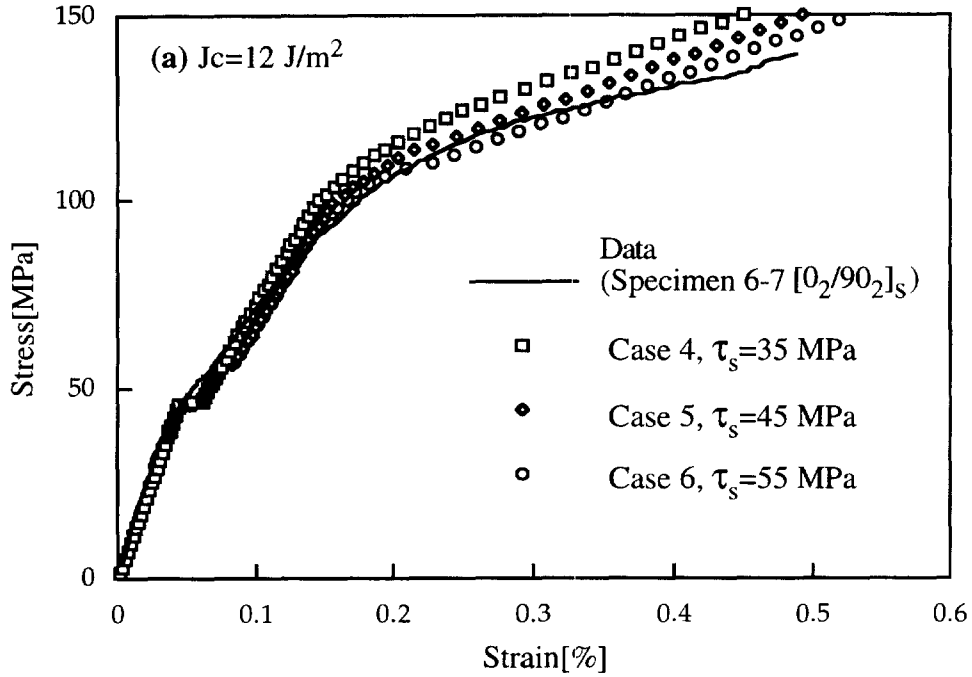

Fig. 18a. Stress–strain response of a $[0_2/90_2]_S$ laminate bilinear slip analyses, $J_c = 12$ J/m^2.

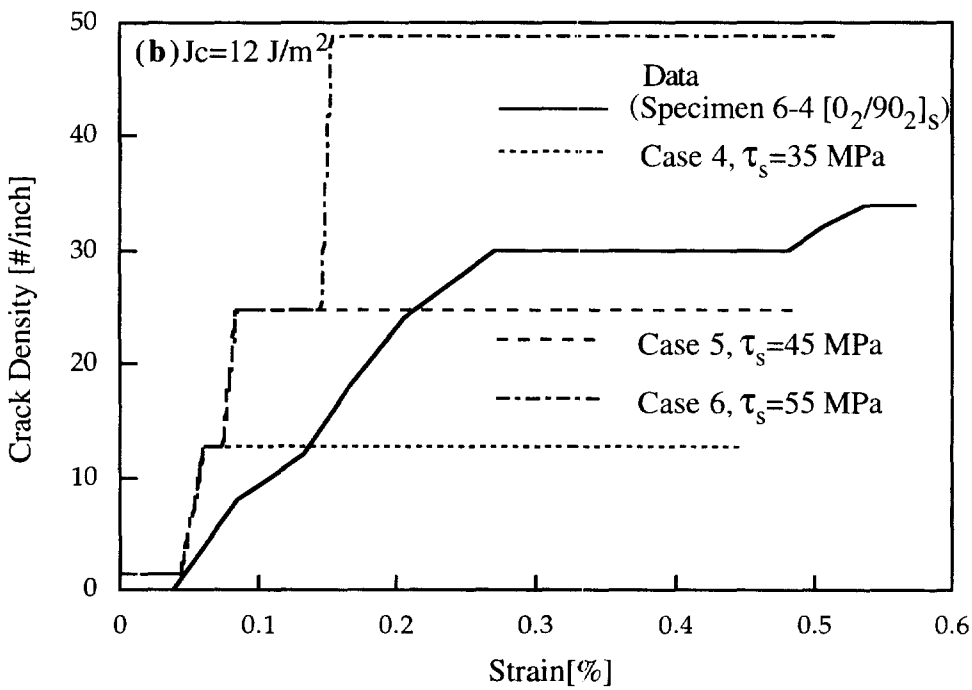

Fig. 18b. Transverse crack accumulation for a $[0_2/90_2]_S$ laminate bilinear slip analyses, $J_c = 12$ J/m$_2$.

5. CONCLUDING REMARKS

The response of SiC/CAS ceramic matrix composites was analyzed by means of an extended shear-lag model. The non-linear stress–strain behavior of the laminate was associated with the non-linear response of the 0° plies and the evolution of transverse cracks within the 90° plies. The formation of the foregoing cracks was predicted by a fracture-energy criterion. To attain good agreement between model predictions and experimental

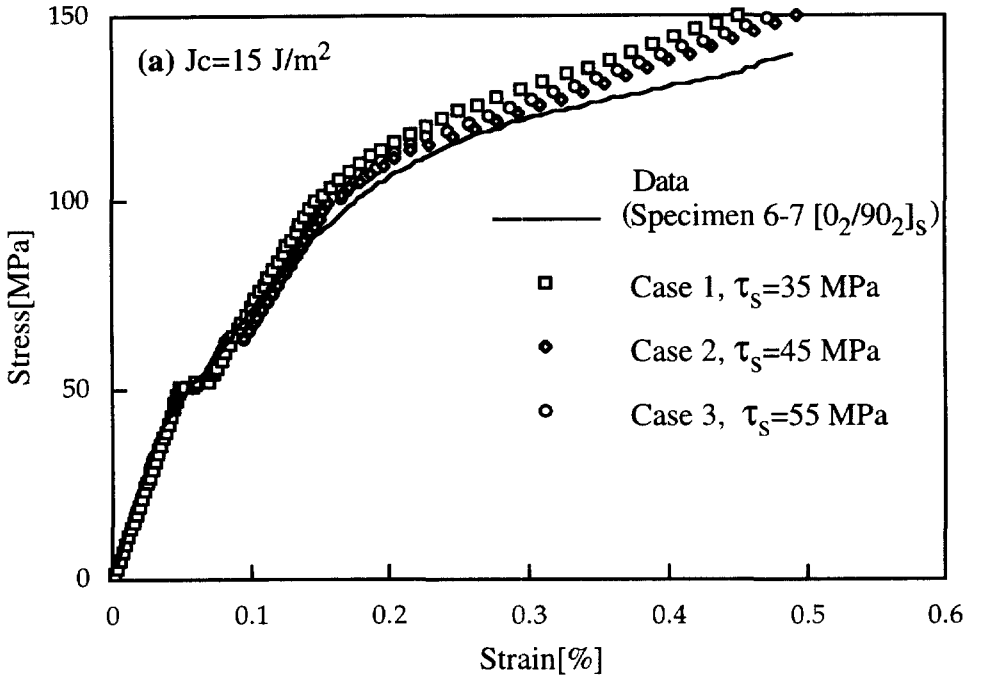

Fig. 19a. Transverse crack accumulation for a $[0_2/90_2]_s$ laminate bilinear slip analyses, $J_c = 15$ J/m^2.

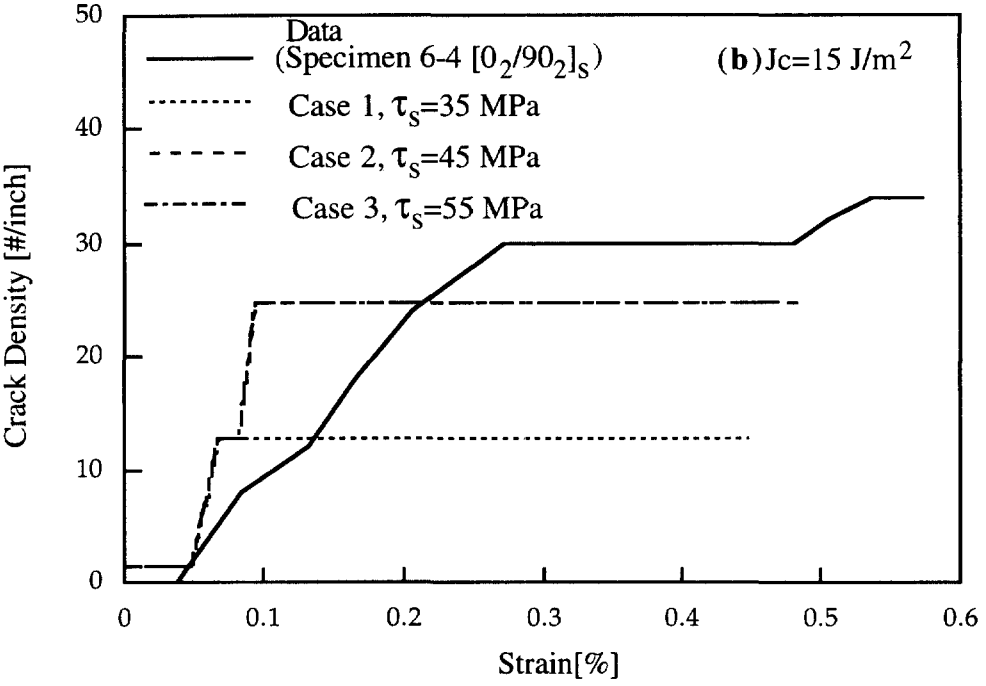

Fig. 19b. Transverse crack accumulation for a $[0_2/90_2]_s$ laminate, bilinear slip analyses $J_c = 15$ J/m^2.

observations it was necessary to include interfacial slip between the 0 and 90° ply groups. For this purpose, an assessment of the interfacial shearing strength was obtained from "push-in" data collected by means of a custom made inter-ply shear fixture.

Satisfactory correlations between model predictions and experimental data were achieved for both the $[0_2/90_2]_s$ and $[0_2/90_4]_s$ cross-ply lay-ups employing reasonable values

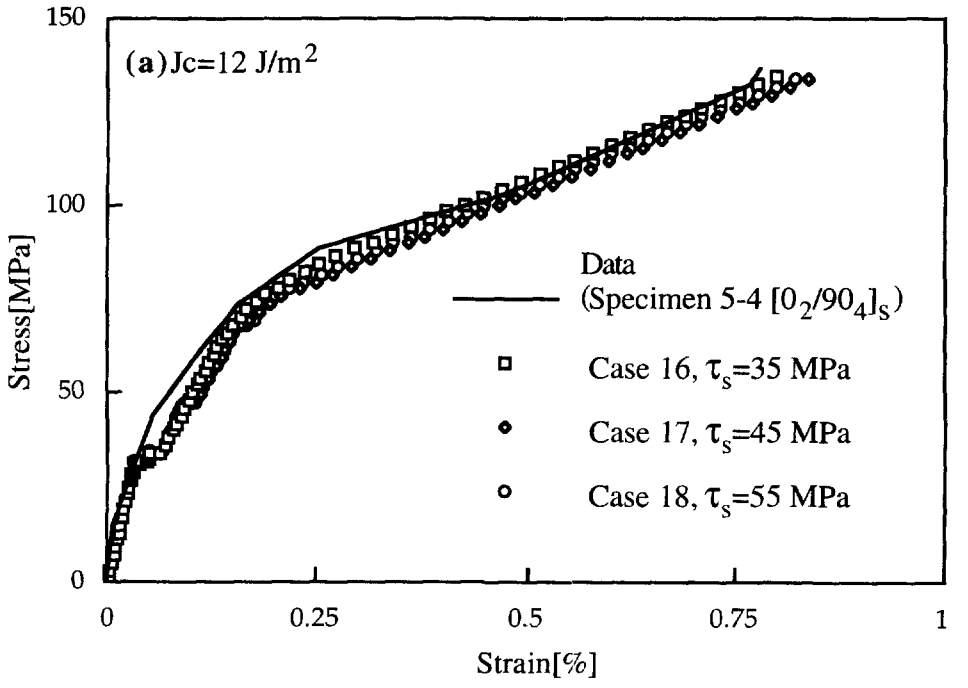

Fig. 20a. Stress–strain response of a $[0_2/90_4]_s$ laminate for bilinear slip analyses, $J_c = 12$ J/m^2.

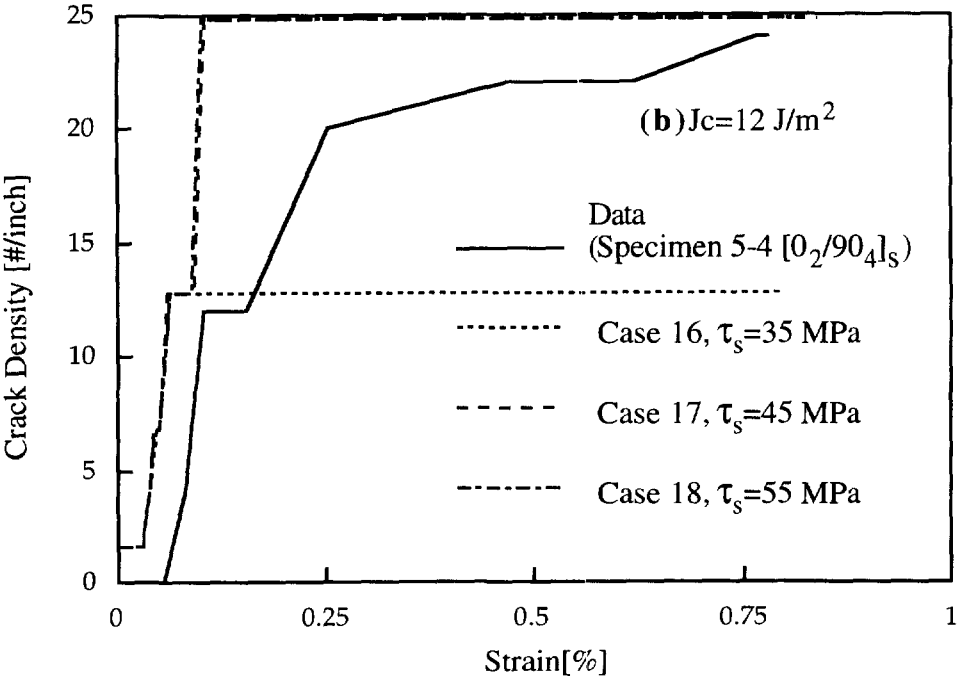

Fig. 20b. Transverse crack accumulation for a $[0_2/90_4]_s$ laminate bilinear slip analyses, $J_c = 12$ J/m^2.

of $J_c \sim 15$ J/m^2 and $\tau_s^* \sim 50$ MPa, which fall within the acceptable range of recorded data.

Note that the current model assumes that all cracks are equally spaced at an initial distance of $2L$, and upon reaching criticality ($J = J_c$), they all split in unison resulting in a new uniform spacing of L. This assumption is, obviously, an unrealistic idealization. A reasonable improvement may be achieved by considering a non-uniform crack spacing, λ

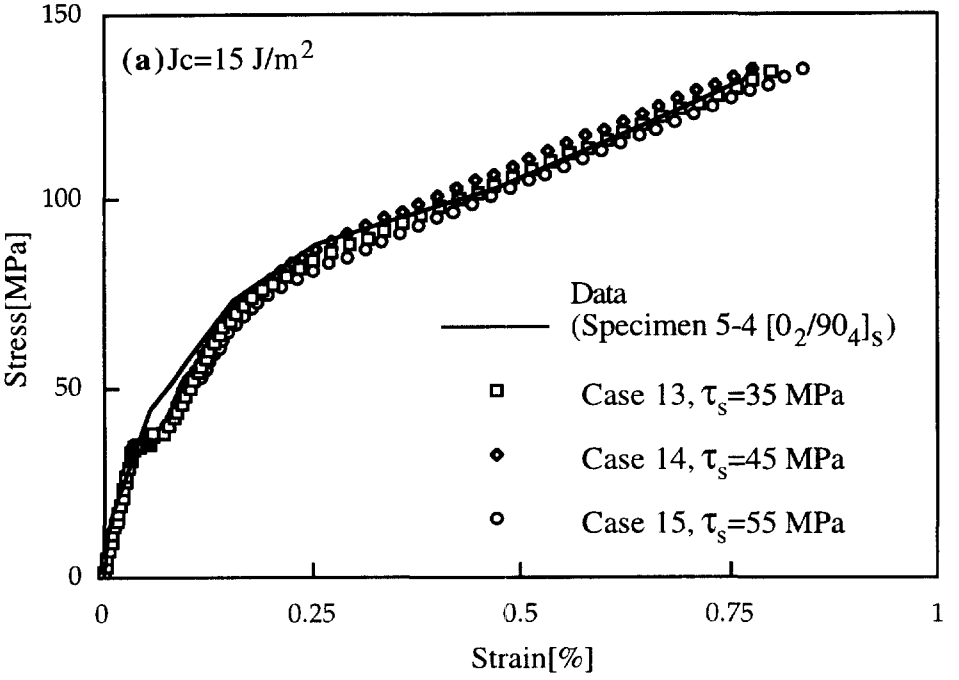

Fig. 21a. Stress–strain response of a $[0_2/90_4]_s$ laminate for bilinear slip analyses, $J_c = 15$ J/m^2.

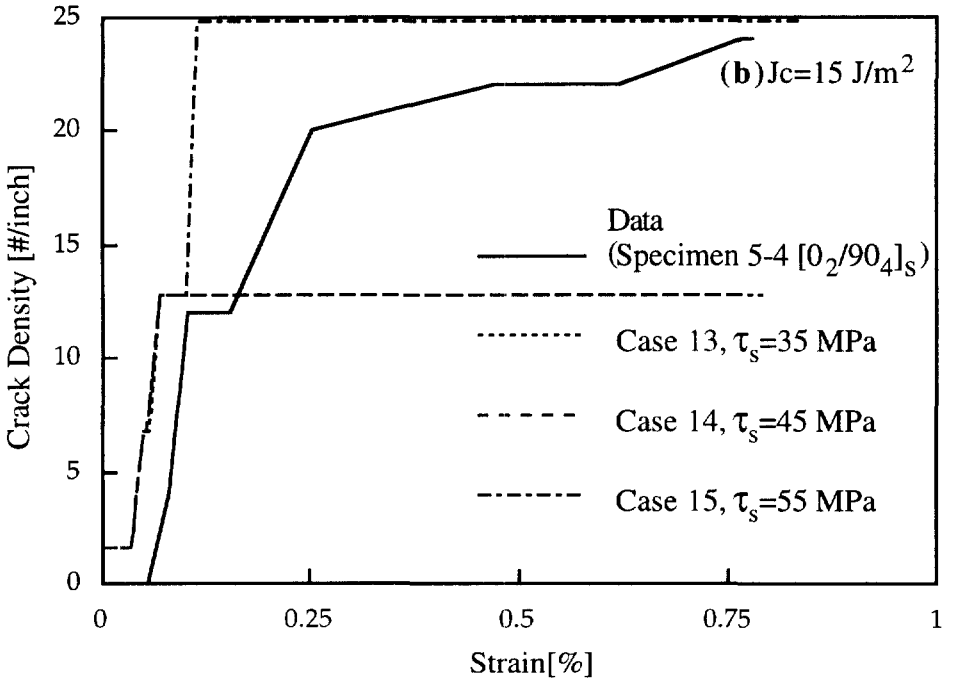

Fig. 21b. Transverse crack accumulation for a $[0_2/90_4]_s$ laminate bilinear slip analyses, $J_c = 15$ J/m^2.

ranging over $L < \lambda \leqslant 2L$. Then the formation of new transverse cracks would occur only within the largest spacings, namely at $\lambda = 2L$.

This revised assumption implies that when crack spacings switch from $2L$ to L the commensurate average crack spacings are $\bar{\lambda} = [3(2L)/4]$ and $\bar{\lambda} = [3(L)/4]$, respectively,

† The selection of a lower limit of $\lambda = L$ is motivated by the assumption of a common value of J_c throughout the laminate. For example, consider $\lambda_{min} = kL$ with $k < l$, then this would imply that cracks spaced at $\lambda = 2kL < 2L$ will split before those spaced at $\lambda = 2L$.

when compared with the aforementioned assumption of uniform crack spacings of $2L$ and L. This implies the existence of 33% more cracks when $\lambda_{max} = 2L$ and 33% fewer cracks when $\lambda_{max} = 2L$ subdivides into $\lambda_{min} = L$. Consequently, the foregoing assumption overestimates the stiffness at λ_{max} and underestimates the stiffness at λ_{min}. Since new transverse cracks are assumed to occur continuously at all load levels, the discontinuities in the predicted curves in Figs 11, 13–15, and 18–21 would be replaced by continuous curves, which should better approximate the experimental data.

REFERENCES

Aveston, J. and Kelly, A. (1973) The theory of multiple fracture of fibrous composites. *Journal of Materials Science* **8,** 352–362.

Aveston, J., Cooper, G. A. and Kelly, A. (1971) Single and multiple fracture. *The Properties of Fibre Composites, Conference Proceedings*. National Physical Laboratory, IPC Science and Technology Press Ltd, pp. 15–26.

Baaklini, G. Y. and Bhatt, R. T. (19??) Failure analysis of SiC/RSBN composite using X-ray monitoring. *4th HITEMP*. pp. 73.1–73.16. NASA CD-91-56650.

Ballarini, R. and Ahmed, S. (1989) Finite element modeling of frictionally restrained composite interfaces. Lewis Research Ctr, Grant NAG3-8956, Contract Report 182281.

Bhatt, R. T. and Phillips, R. E. (1988) Laminate behavior for SiC fiber-reinforced reaction-bonded silicon nitride matrix composites. NASA Technical Memorandum 101350.

Brennan, J. J. and Prewo, K. M. (1982) Silicon carbide fibre reinforced glass–ceramic matrix composites exhibiting high strength and toughness. *Journal of Materials Science* **17,** 2371–2383.

Bright, J. D., Shetty, D. K., Griffin, C. W. and Limaye, S. Y. (1989) Interfacial bonding and friction in silicon carbide (filament)-reinforced ceramic- and glass–matrix composites. *Journal of the American Ceramic Society* **72**(5), 746–753.

Budiansky, B. (1993) On the theoretical toughness and strength of ceramic composites. *Proceedings of IUTAM Symposium on Fracture of Brittle Disordered Materials: Concrete, Rock, Ceramics*. Brisbane, to be published.

Budiansky, B. and Cui, Y. L. (1994) On the tensile strength of a fiber-reinforcement ceramic composite containing a crack-like flaw. *Journal of the Mechanics and Physics of Solids* **42**(1), 1–19.

Budiansky, B., Evans, A. G. and Hutchinson, J. W. (1994) Fiber–matrix debonding effects on the cracking in aligned-fiber ceramic composites. MECH-233, Harvard University, Division of Applied Sciences. Cambridge, MA.

Budiansky, B., Hutchchinson, J. W. and Evans, A. G. (1986) Matrix fracture in fiber-reinforced ceramics. *Journal of the Mechanics and Physics of Solids* **35,** 167–189.

Cao, H. C. (1990) Tensile tests of ceramic matrix composites: theory and experiment. *Journal of the American Ceramic Society* **73**(7), 2091–2094.

Chan, K. S., He, M. Y. and Hutchchinson, J. W. (1993) Cracking and stress redistribution in ceramic layered composites. *Material Sciences and Engineering* **A167,** 57–64.

Charalambides, P. G. and Evans, A. G. (1989) Debonding properties of residually stresses brittle–matrix composites. *Journal of the American Ceramic Society* **72**(10), 1891–1898.

Chulya, A., Geyekenyesi, J. P. and Bhatt, R. T. (1991) Mechanical behavior of fiber reinforced SiC/RBSN ceramic matrix composites: theory and experiments. NASA Technical Memorandum 103688.

Cui, Y. L. (1993) On the strength of fiber-reinforced ceramic composites containing an elliptical hole. MECH-217. Harvard University, Division of Applied Sciences, Cambridge, MA.

Cui, Y. L. and Budiansky, B. (1993) Steady-state matrix cracking of ceramics reinforced by aligned fibers and transforming particles. *Journal of the Mechanics and Physics of Solids* **41**(4), 615–630.

Daniel, I. M. (1995) Failure mechanisms and damage evolution in crossply ceramic matrix composites. *International Journal of Solids and Structures* **32**(3–4), 341–355.

Daniel, I. M., Anastassopoulos, G. and Lee, J. W. (1989) Experimental micromechanics of brittle matrix composites. In *Micromechanics: Experimental Techniques*. ASME. AMD-Vol. 102, pp. 133–146.

Daniel, I. M., Anastassopoulos, G. and Lee, J. W. (1992) Failure mechanisms and interfacial shear strength in brittle-matrix composites. ASME AD-Vol.29/AMD-Vol. 146. *Advances in Experimental Mechanics and Biomeimetics*, pp. 57–69.

Davidson, D. L., Rosseau, C. Q. and Campbell, J. B. (19??) The micromechanics of ambient temperature cyclic loading fatigue in a composite of CAS glass ceramic reinforced with nicalon fibers. *Acta Metall.* (11–91), submitted.

Deshmukh, U. V. and Coyle, T. W. (1988) Determination of the interface strength in glass–SiC composites via single fiber tensile testing. *Ceramic Engineering Science Proceedings* 9 (7–8), 627–634.

Erdman, D. L. and Weitsman, Y. J. (1996) The multi-fracture response of cross-ply ceramic composites. 20th Annual Cocoa Beach Conference and Exposition on Composites, Advanced Ceramics, Materials and Structures, to be published.

Evans, A. G. (1990) Perspective on the development of high-toughness ceramics. *Journal of the American Ceramic Society* **73**(2), 187–206.

He, M. Y., Wu, B.-X. and Evans, A. G. (1993) Inelastic strains due to matrix cracking in unidirectional fiber reinforced composites. MECH-222, Harvard University, Division of Applied Sciences, Cambridge, MA.

Hillig, W. B. (1987) Strength and toughness of ceramic matrix composites. *Am. Rev. Mater. Sci.* **17,** 341–383.

Schioler, L. J. and Stiglich, J. J. Jr (1986) Ceramic matrix composites: a literature review. *Ceramic Bulletin* **65**(2), 289–292.

Hsueh, C.-H. (1989) Some considerations of evaluation of interfacial frictional stress from the indentation technique for fibre-reinforced ceramic composites. *Journal of Materials Science Letters* **8,** 739–742.

Hsueh, C.-H. (1990) Evaluation of interfacial shear strength, residual clamping stress and coefficient of friction for fiber-reinforced ceramic composites. *Acta metall. mater.*, **38**(3), 403–409.
Karandikar, P. and Chou, T.-W. (1992) Characterization and modeling of microcracking and elastic moduli changes in Nicalon–CAS composites. *Composite Science and Tech.* Center for Composite Materials and Material Science Program, University of Delaware, to be published.
Kerans, R. J., Hay, R. S. and Pagano, N. J. (1989) The role of the fiber–matrix interface in ceramic composites. *American Ceramic Society Bulletin* **68**(2), 429–442.
Kim, R. Y. (1992) Experimental observation of progressive damage in SiC/Glass–Ceramic Composites. *ACSS Proceedings of the 16th Annual Conference on Composites and Advanced Ceramics Material* **13**(7–8), 281–300.
Kuo, W.-S. and Chou, T.-W. (1990) Mechanical behaviors of ceramic matrix composites with matrix cracking and fiber debonding. *5th Japan–US Conference on Composites*, Tokyo, Japan.
Kuo, W.-S. and Chou, T.-W. (1992) Modeling of damage in ceramic matrix cross-ply composites. *Damage Mechanics and Localization*, AMD-Vol 142/MD-Vol. 34, pp. 97–107. ASME.
Kuo, W.-S. and Chou, T.-W. (19??) Multiple cracking of unidirectional and cross-ply ceramic matrix composites. Center for Composite Materials and Department of Mechanical Engineering, University of Delaware, Newark, DE, to be published.
Larsen, C. G. (1990) Ceramics tensile grip. *Thermal and Mechanical Behavior of Metal Matrix and Ceramic Matrix Composites*. ASTM, STP 1080, pp. 235–246.
Lu, M.-C. and Hsueh, C.-H. (1990) Effects of friction in ceramic coating/fiber composites. *Journal of Composite Materials* **24,** 572–593.
Lu, T. J. and Hutchinson, J. W. (1994) Effect of matrix cracking and interface sliding on the thermal expansion of fiber-reinforced composites. MECH-231. Harvard University, Division of Applied Sciences, Cambridge, MA.
Marshall, D. B. (1984) An indentation method for measuring matrix–fiber frictional stresses in ceramic composites. *Communications of the American Ceramic Society*, pp. C259–260.
Marshall, D. B. (1987) Interfaces in ceramic matrix composites. *Materials Science Research* **21,** (Ceramic Microstructures 1986). Plenum Press, New York and London.
Nardone, V. C. and Prewo, K. M. (1988) Tensile performance of carbon-fibre-reinforced glass. *Journal of Materials Science* **23,** 168–180.
Phillips, D. C. (1974) Interfacial bonding and the toughness of carbon-fibre-reinforced glass and glass-ceramics. *Journal of Materials Science* **9,** 1847–1854.
Prewo, K. M. (1987) Fatigue and stress rupture of silicon carbide fiber-reinforced glass–ceramics. *Journal of Materials Science* **22,** 2695–2701.
Prewo, K. M. (1986) Tension and flexural strength of silicon carbide fiber-reinforced glass–ceramics. *Journal of Materials Science* **21,** 3590–3600.
Prewo, K. M. and Brennan, J. J. (1980) High-strength silicon carbide in fibre-reinforced glass–matrix composites. *Journal of Materials Science* **15,** 463–468.
Prewo, K. M. and Brennan, J. J. (1982) Silicon carbide yarn reinforced glass–matrix composites. *Journal of Materials Science* **17,** 1201–1206.
Pryce, A. W. and Smith, P. A. (1991) Matrix cracking in ceramic matrix composites under quasi-static tensile loading. *Proceedings of the Eighth International Conference on Composite Materials* (ICCM/8), 15–19 July, pp. 24-A-1–24-A-10.
Rousseau, C. Q. (19??) Monotonic and cyclic behavior of a silicon carbide/calcium–aluminosilicate ceramic composite. *Thermal and Mechanical Behavior of Metal Matrix and Ceramic Matrix Composites*, ASTM STP 1080, pp. 136–151.
Singh, R. N. (1989) Fiber–matrix interfacial characteristics in a fiber-reinforced ceramic matrix composite. *Ceram. Eng. Sci. Proc.* **10**(7–8), 883–893.
Walter, M. E. (1995) An experimental investigation of damage evolution in a ceramic matrix composite. *Journal of Engineering Materials and Technology* **117,** 101–108.
Xia, Z. C., Carr, R. R. and Hutchinson, J. W. (1993) Matrix cracking of cross-ply ceramic composites. MECH-218, Harvard University, Division of Applied Sciences, Cambridge, MA.
Xia, Z. C., Carr, R. R. and Hutchinson, J. W. (1993) Transverse matrix cracking in fiber-reinforced brittle matrix, cross-ply laminates. *Acta metall. mater.* **41**(8), 2365–2376.

APPENDIX

Carrying out the integration in (15) results in the following expression for the transverse strain:

$$\bar{\varepsilon}_y = \frac{-\bar{\sigma}_x(C_3\bar{h}L+\beta_1 k_1 k_3)}{\beta_1 k_1 k_4 + L(C_2 h_1 + C_4 h_2)} \tag{A1}$$

where

$$C_1 = Q_{12}^{(1)}/Q_{11}^{(1)}, \qquad C_2 = Q_{22}^{(1)} - (Q_{12}^{(1)})^2/Q_{11}^{(1)}, \qquad C_3 = Q_{12}^{(2)}/Q_{11}^{(2)}, \qquad C_4 = Q_{22}^{(2)} - (Q_{12}^{(2)})^2/Q_{11}^{(2)}$$

and

$$\beta_1 = \frac{(C_1 - C_3)}{\alpha_0}\left(L\cosh(\alpha_0 L) - \frac{\sinh(\alpha_0 L)}{\alpha_0}\right)$$

$$k_1 = A_{55}/(\bar{h}\alpha_0 Q_{11}^{(1)} Q_{11}^{(2)} \cosh(\alpha_0 L))$$

$$k_3 = \frac{\bar{h} Q_{11}^{(1)}}{h_2}$$

$$k_4 = Q_{12}^{(1)} Q_{11}^{(2)} - Q_{12}^{(2)} Q_{11}^{(1)}$$

In the case of the non-linear response of the 0° plies, the expressions for A_1, B_1 are obtained through use of the boundary conditions in (12), (13) and (27):

$$\begin{Bmatrix} A_1 \\ B_1 \end{Bmatrix} = \frac{1}{D}\begin{bmatrix} \cosh(\alpha_1 x^*) & -\alpha_1 \sinh(\alpha_1 L) \\ -\sinh(\alpha_1 x^*) & \alpha_1 \cosh(\alpha_1 L) \end{bmatrix}\begin{Bmatrix} k_5 \bar{\sigma}_x + k_6 \bar{\varepsilon}_y - k_7 \\ A_0 \sinh(\alpha_0 x^*) \end{Bmatrix} \tag{A2}$$

where

$$D = \alpha_1 \cosh(\alpha_1 (L - x^*))$$

Employing (15) for the bilinear case, $\bar{\varepsilon}_y$ is given as:

$$\bar{\varepsilon}_y = \frac{\begin{Bmatrix} h_2 C_7 (L - x^*) + h_1 [C_3\beta_6 + C_5\beta_9 - C_1(\beta_6 + \beta_9)] \\ -\bar{\sigma}_x [h_1 C_1(\beta_4 + \beta_7) - h_1 C_3 \beta_4 + \bar{h} C_3 x^* + \bar{h} C_5 (L - x^*) - h_1 C_5 \beta_1] \end{Bmatrix}}{\{h_1 (C_2 L + C_1(\beta_5 + \beta_8) - C_3\beta_5 - C_5\beta_8) + h_2 (C_4 x^* + C_6 (L - x^*))\}} \tag{A3}$$

Note that k_4 and $C_1 - C_4$ are the same as in the previous solution while the newly introduced constants in (A3) are given by:

$$\hat{k}_1 = \frac{A_{55}}{\bar{h}\alpha_0 Q_{11}^{(1)} Q_{11}^{(2)} \cosh(\alpha_0 x^*)} \qquad k_5 = \frac{A_{55}}{\tilde{Q}_{11}^{(2)} h_2}$$

$$k_2 = \sigma_0 \left(Q_{11}^{(1)} + \frac{h_2}{h_1} Q_{11}^{(2)}\right) \qquad k_6 = \frac{A_{55}}{\bar{h}}\left(\frac{Q_{12}^{(1)}}{Q_{11}^{(1)}} - \frac{Q_{12}^{(2)}}{\tilde{Q}_{11}^{(2)}}\right)$$

$$\hat{k}_3 = \frac{\bar{h} Q_{11}^{(2)}}{h_1} \qquad k_7 = \frac{A_{55}}{\bar{h}} \frac{\hat{\sigma}}{\tilde{Q}_{11}^{(2)}}$$

$$C_5 = Q_{12}^{(2)}/\tilde{Q}_{11}^{(2)}, \qquad C_6 = Q_{22}^{(2)} - (Q_{12}^{(2)})^2/\tilde{Q}_{11}^{(2)}, \qquad C_7 = Q_{12}^{(2)}\hat{\sigma}/\tilde{Q}_{11}^{(2)}$$

while

$$\hat{\beta}_1 = x^* \cosh(\alpha_0 x^*) - \sinh(\alpha_0 x^*)/\alpha_0$$

$$\beta_2 = (L - x^*)\cosh(\alpha_1 L) - \sinh(\alpha_1 L)/\alpha_1 + \sinh(\alpha_1 x^*)/\alpha_1$$

$$\beta_3 = (L - x^*)\sinh(\alpha_1 L) - \cosh(\alpha_1 L)/\alpha_1 + \cosh(\alpha_1 x^*)/\alpha_1$$

$$\beta_4 = \frac{\bar{h} x^*}{h_1} - \frac{\hat{k}_1 \hat{k}_3 \hat{\beta}_1}{h_1 \alpha_0} \qquad \beta_7 = \frac{\gamma_1\beta_2 + \gamma_4\beta_3}{h_1\alpha_1}$$

$$\beta_5 = \frac{\hat{k}_1 k_4 \hat{\beta}_1}{h_1 \alpha_0} \qquad \beta_8 = \frac{\gamma_2\beta_2 + \gamma_5\beta_3}{h_2\alpha_1}$$

$$\beta_6 = \frac{\hat{k}_1 k_2 \hat{\beta}_1}{h_1 \alpha_0} - \frac{\sigma_0 h_2 x^*}{h_1} \qquad \beta_9 = \frac{\gamma_3\beta_2 + \gamma_6\beta_3}{h_1\alpha_1}$$

$$\begin{Bmatrix} \gamma_1 \\ \gamma_2 \\ \gamma_3 \end{Bmatrix} = \frac{1}{D}\begin{bmatrix} k_5 & \hat{k}_1\hat{k}_3\alpha_1 \\ k_6 & -\hat{k}_1 k_4 \alpha_1 \\ -k_7 & -\hat{k}_1 k_2 \alpha_1 \end{bmatrix}\begin{Bmatrix} \cosh(\alpha_1 x^*) \\ \sinh(\alpha_1 L)\sinh(\alpha_0 x^*) \end{Bmatrix}$$

$$\begin{Bmatrix} \gamma_4 \\ \gamma_5 \\ \gamma_6 \end{Bmatrix} = \frac{1}{D}\begin{bmatrix} -k_5 & -\hat{k}_1\hat{k}_3\alpha_1 \\ -k_6 & \hat{k}_1 k_4 \alpha_1 \\ k_7 & \hat{k}_1 k_2 \alpha_1 \end{bmatrix}\begin{Bmatrix} \sinh(\alpha\ x^*) \\ \cosh(\alpha_1 L)\sinh(\alpha_0 x^*) \end{Bmatrix}$$

In the circumstance that non-linear response of the 0° plies is accompanied by interfacial slippage, "Case I" ($L-l_s < x^*$) we have:

$$A_0 = \hat{k}_1(k_3\bar{\sigma}_x + k_4\bar{\varepsilon}_y) - k_8 \tag{A4}$$

with

$$\hat{k}_1 = A_{55}/(\bar{h}\alpha_0 Q_{11}^{(1)} Q_{11}^{(2)} \cosh(\alpha_0(L-l_s))$$

$$k_8 = \frac{\tau_s^* \eta_s \alpha_0}{\cosh(\alpha_0(L-l_s))}$$

For the situation where non-linear response of the 0° plies is accompanied by interfacial slippage, "Case II" ($L-l_s > x^*$) we have:

$$A_0 = \hat{k}_1(k_2 - \hat{k}_3\bar{\sigma}_x + k_4\bar{\varepsilon}_y) \tag{A5}$$

The values of A_1 and B_1 for this case are given by:

$$\begin{Bmatrix} A_1 \\ B_1 \end{Bmatrix} = \frac{1}{\hat{D}} \begin{bmatrix} \cosh(\alpha_1 x^*) & -\alpha_1 \sinh(\alpha_1(L-l_s)) \\ -\sinh(\alpha_1 x^*) & \alpha_1 \cosh(\alpha_1(L-l_s)) \end{bmatrix} \begin{Bmatrix} k_5\bar{\sigma}_x + k_6\bar{\varepsilon}_y - \hat{k}_7 \\ A_0 \sinh(\alpha_0 x^*) \end{Bmatrix} \tag{A6}$$

with

$$\hat{D} = \alpha_1 \cosh(\alpha_1(L-l_s-x^*))$$

$$\hat{k}_7 = \frac{A_{55}\hat{\sigma}}{\bar{h}\bar{Q}_{11}^{(2)}} + \tau_s^* \eta_s \alpha_1^2$$

The expression for $\bar{\varepsilon}_y$ is then given as:

$$\bar{\varepsilon}_y = \frac{\begin{array}{l} C_7 h_2(L-x^*) - h_1(C_1 - C_5)(\hat{\beta}_9 + \beta_{10}) - h_1\beta_6(C_1 - C_3) \\ -\bar{\sigma}_x\{h_1\beta_4(C_1 - C_3) + h_1\hat{\beta}_7(C_1 - C_5) + C_3\bar{h}x^* + C_5\bar{h}(L-x^*)\} \end{array}}{\{h_1\beta_5(C_1 - C_3) + h_1\hat{\beta}_8(C_1 - C_5) + h_1 C_2 L + h_2 C_4 x^* + h_2 C_6(L-x^*)\}} \tag{A7}$$

where

$$\hat{\beta}_2 = (L-l_s-x^*)\cosh(\alpha_1(L-l_s)) - \sinh(\alpha_1(L-l_s))/\alpha_1 + \sinh(\alpha_1 x^*)/\alpha_1$$

$$\hat{\beta}_3 = (L-l_s-x^*)\sinh(\alpha_1(L-l_s)) - \cosh(\alpha_1(L-l_s))/\alpha_1 + \cosh(\alpha_1 x^*)/\alpha_1$$

$$\hat{\beta}_7 = \frac{\hat{\gamma}_1\hat{\beta}_2 + \hat{\gamma}_4\hat{\beta}_3}{h_1\alpha_1}, \qquad \hat{\beta}_8 = \frac{\hat{\gamma}_2\hat{\beta}_2 + \hat{\gamma}_5\hat{\beta}_3}{h_1\alpha_1}$$

$$\hat{\beta}_9 = \frac{\hat{\gamma}_3\hat{\beta}_2 + \hat{\gamma}_6\hat{\beta}_3}{h_1\alpha_1} + \frac{\tau_s^*\eta_s(L-l_s-x^*)}{h_1}, \qquad \beta_{10} = \frac{\tau_s^*\eta_s^2}{2h_1}$$

$$\begin{Bmatrix} \hat{\gamma}_1 \\ \hat{\gamma}_2 \\ \hat{\gamma}_3 \end{Bmatrix} = \frac{1}{\hat{D}} \begin{bmatrix} k_5 & \hat{k}_1\hat{k}_3\alpha_1 \\ k_6 & -\hat{k}_1 k_4 \alpha_1 \\ -k_7 & -\hat{k}_1 k_2 \alpha_1 \end{bmatrix} \begin{Bmatrix} \cosh(\alpha_1 x^*) \\ \sinh(\alpha_1(L-l_s)\sinh(\alpha_0 x^*) \end{Bmatrix}$$

and

$$\begin{Bmatrix} \hat{\gamma}_4 \\ \hat{\gamma}_5 \\ \hat{\gamma}_6 \end{Bmatrix} = \frac{1}{\hat{D}} \begin{bmatrix} -k_5 & -\hat{k}_1\hat{k}_3\alpha_1 \\ -k_6 & \hat{k}_1 k_4 \alpha_1 \\ k_7 & \hat{k}_1 k_2 \alpha_1 \end{bmatrix} \begin{Bmatrix} \sinh(\alpha_1 x^*) \\ \cosh(\alpha_1(L-l_s))\sinh(\alpha_0 x^*) \end{Bmatrix}$$

For Case III of the slip analysis we have:

$$A_0 = \check{k}_1(k_3\bar{\sigma}_x + \check{k}_4\bar{\varepsilon}_y - \check{k}_5) - \check{k}_8 \tag{A8}$$

with

$$\check{k}_1 = A_{55}/(\bar{h}\alpha_1 Q_{11}^{(1)}\tilde{Q}_{11}^{(2)}\cosh(\alpha_1(L-l_s)))$$

$$\check{k}_4 = Q_{12}^{(1)}\tilde{Q}_{11}^{(2)} - Q_{12}^{(2)}Q_{11}^{(1)}$$

$$\check{k}_5 = Q_{11}^{(1)}\hat{\sigma}$$

$$\check{k}_8 = \frac{\tau_s^{sat}\alpha_1}{\cosh(\alpha_1(L-l_s))}$$

and the transverse strain is given as:

$$\bar{\varepsilon}_s = \frac{h_2 C_7 L - C_5\bar{\sigma}_s\bar{h}L + (C_5 - C_1)\left(\check{k}_1\check{k}_3\check{\beta}_1\bar{\sigma}_s - \check{k}_1\check{k}_6\check{\beta}_1 - \check{k}_8\check{\beta}_1 + \tau_s^{sat}(L-l_s) + \frac{\tau_s^{sat}l_s^2}{2}\right)}{L(h_1C_2 + h_2C_6) + (C_1 - C_3)\check{k}_1\check{k}_4\check{\beta}_1} \tag{A9}$$

with

$$\check{\beta}_1 = \frac{1}{\alpha_1}\{(L-l_s)\cosh(\alpha_1(L-l_s)) - \sinh(\alpha_1(L-l_s))/\alpha_1\}$$